2019

Numerical Investigation of Composite Floor Beam Resilience to Realistic Fire Scenarios

Michael Drury
Lehigh University

Numerical Investigation of Composite Floor Beam Resilience to Realistic Fire Scenarios

by

Michael M. Drury

Advised by Dr. Spencer Quiel

A Thesis

Presented to the Graduate and Research Committee

Of Lehigh University

In Candidacy for the Degree of

Master of Science

In Structural Engineering

Lehigh University

August 2019

This thesis is accepted and approved in partial fulfillment of the requirements for the Master of Science.

_____
Date

_____
Spencer E. Quiel
Thesis Advisor

_____
Panayiotis Diplas
Chairperson of Department

Acknowledgements

The author extends his sincere gratitude to his wife, Kaitlyn, his mother, Renata, his stepfather, Kerry, and his brother, John for their support throughout his career in education and life in general. The author would like to thank his advisor Dr. Spencer Quiel, for his knowledge, guidance, and consistent positive outlook on all aspects of the research. The author also thanks his fellow graduate students at ATLSS for their support and advice along the way. The author gratefully acknowledges the funding provided by Lehigh University for his first year of graduate study, as well as the sponsors of his research project, the American Institute of Steel Construction and the Pennsylvania Infrastructure Technology Alliance.

Table of Contents

List of Tables

List of Figures

Abstract

This thesis provides a computational investigation of three separate composite steel beam fire tests conducted at Lehigh University's ATLSS Laboratory as well as parametric analyses with various fire curves and levels of passive protection. The objective of this study was to validate numerical models that conservatively capture structural failure of composite floors subjected to fire, while striving for simplicity, to help further realize performance-based design and evaluation approaches for structural-fire resistance and resilience of secondary floor framing in steel buildings.

The first pair of tests were identical structural systems with one having passive fire protection and the other being unprotected subjected to the ASTM E119 fire curve. Thermal analysis of the steel was performed using a lumped mass approach, which can be implemented via spreadsheet or a simple, explicit programmed solution. Thermal analysis of the slab was performed using a simple one-dimensional heat flow model. Two types of finite element analyses were performed: one composed of shell elements and another composed of fiber-beam elements. The slab was unrestrained in all cases, so the effects of slab continuity and membrane action were neglected. The structural models referenced both lumped mass prediction temperatures as well as measured test temperatures as input for the temperature-dependent material properties of the specimens. The results of all models show conservative agreement with the experimentally observed behavior. The plasticity of the section is analyzed over the duration of the tests using the concept of warping axial-moment failure envelopes which consider shifting of the effective centroid due to the thermal gradient per three-sided heating. These models can be leveraged as part

of a conservative performance-based approach to design composite floor assemblies for one-way flexural behavior under fire.

The final validation case consisted of an unprotected composite beam subjected to a realistic fire curve with a decay phase. The objective of this study was to point towards the possibility of surviving a realistic fire scenario with a decay phase, as opposed to the continued growth of the ASTM E119 curve. The test fire curve closely matches the E119 fire for 20 minutes prior to rapidly decaying. The test beam was shown to withstand the parametric fire curve computationally, resulting in relatively little damage, matching the test observations reported. According to the ASTM E119 thermal criteria, the beam "failed" around 13 minutes. The same pair of SAFIR finite element models used in the runaway failure model validation were used to compare structural behavior of an assembly when it is permitted to cool in the case of fire suppression.

The models of the realistic fire test were then parametrically extended to various combinations of active and passive protection, as well as different fire curve formulations. The fact that these models could capture failure per the first validation study allowed for this extension to be confidently applied. The model comparisons highlight the current E119 standard's lack of resiliency quantification. The standard may have potential to be used as a benchmarking tool in resiliency calculations, in turn making use of the plethora of data that has already been obtained over the last several decades.

1.0 Introduction

Currently, steel buildings in the US are protected from fire using prescriptive considerations, by which passive and active fire protection measures are selected according to provisions stated in the International Building Code (IBC) [1], usually by architects. Active fire protection is typically employed using sprinkler systems, and passive fire protection often consists of coating materials that are applied to the structural elements after erection or encasement. Based on the building category and size the 2018 IBC requires an hourly rating of applied passive fire protection to be met. The passive protection quantity is predicated on the results of experimental tests referred to as "standard" fire tests, such as ASTM E119 [2] and ISO 834 [3]. The tested assemblies, such as those documented in the UL product specification catalog [4], are assigned hourly ratings determined using limits on the temperature increase in the steel and/or the rate/magnitude of load-induced deflection. Nearly all composite floor assemblies in steel buildings (most consisting of wide-flange steel beams connected to a reinforced concrete floor slab via cast-in shear studs) will not exactly match those evaluated via the standard fire test. ASTM E119 conversion equations for translating the fire protection requirements from the tested assemblies to an actual structure in ASCE/SEI/SFPE 29-05 [5] and AISC Design Guide 19 [6] are thermally focused and adjust the required fire protection thickness using the relative ratios of beam size (weight) to fire exposed perimeter (*W/D*).

For many conventional steel buildings, the prescriptive methods may be justified as an efficient and relatively cost effective approach to providing minimum levels of fire resistance if the cost of additional protection is less than the cost of engineering. However, the translation of hourly ratings from standard fire tested specimens to actual composite

floor systems is ambiguous and not necessarily consistent. Previous research has shown that the structural performance of fire-exposed composite beams with fire protection obtained via the ASCE 29-05 conversion can vary based on the load level, span length, steel and slab dimensions, thermal restraint, and fire exposure intensity [7]. Full-scale fire tests of steel-framed buildings at Cardington [8,9] have demonstrated the resistance of unprotected composite floor beams to realistic fire scenarios (which include a decay phase).

In North American practice, prescriptive fire protection requirements for floor systems in steel buildings are classified as either unrestrained or restrained to thermal expansion. Both ASTM E119 [2] and the 2018 IBC [1] stipulate that engineering judgment must be exercised to determine whether the surrounding or supporting structure is sufficient to restrain thermal expansion. There is no standardized method to determine "sufficient restraint" and stiffness will vary on a case-by-case basis making it difficult to relate back to the standard fire test results. Some experimental studies [10,11] have supported the expectation that a typical restrained composite beam subassembly will have a higher hourly rating under fire versus an unrestrained subassembly (making unrestrained the generally conservative assumption despite being unattainable in real construction), while others have indicated that increased restraint may actually induce a faster onset of plastic behavior [12], and optimal fire resistance may be obtained at partial restraint [7].

Performance-based structural-fire analysis methods are permitted as an alternative to the current thickness conversions for fire protection to examine the changes in demand and capacity that occur as a structural member is heated and account for its interaction with the surrounding structure. Per section 703.4.4 of the 2018 IBC, engineering analysis can be used to demonstrate fire resistance equivalent to the prescriptive requirements [1].

Performance-based methods for calculating the behavior of steel structures under fire have been a part of the Eurocode for over a decade [13], and the availability of performance-based provisions is increasing in North American practice via Appendix 4 in AISC 360-16 [14], Appendix E in ASCE 7-16 [15], and ASCE's *Manual of Practice 138: Structural Fire Engineering* [16]. These references state that an analysis of a steel structure's mechanical response to fire must account for both the degradation of the steel material's strength and stiffness due to increased temperatures as well as the effects of thermal expansion and large deflection.

There is currently little guidance regarding the implementation as well as the impact of realistic design parameters in the resulting performance-based analysis. There is also no consensus regarding performance limits or damage levels associated with the calculated response of steel supported floor systems to fire. Prescriptive methods do not consider demand on a case-specific basis or the associated level of damage for a given fire threat. The implementation of a performance-based framework requires the use of reliable and validated engineering models that can be used to make these evaluations in addition to quantifiable limit states to be considered. Fire protection codes currently specify protection according to the occupancy, function, square footage, and height of the building. Increased use of performance-based methods hope to leverage the hourly rating classifications by correlating the ratings to expected damage levels in fires of varying severity. For the purposes of design, acceptable damage levels could be determined for the specific use considered, and an accurate assessment of structural integrity in the event of a fire could be provided. A similar approach is used in current criteria for blast resistant structural

engineering [17], which could be used as a potential model for developing a performance criteria for fire resistance of steel structures.

Using the experimental data from previous work done at Lehigh by Kordosky [18], this work evaluates thermal and structural analysis methods of varying complexity to capture the thermo-mechanical response of composite floor beams to the standard fire and a natural fire. The goal of this modeling effort is to obtain accurate, conservative predictions of fire-induced limit states and survivability at reduced computational cost, thus increasing the accessibility of these methods to practicing engineers. Validation of performance-based calculations against the results of a standard fire test is the first step toward their implementation to engineer as-built composite floor systems at fire resistance levels consistent with as-tested specimens. With the standard fire results computationally replicated, realistic models can aim to leverage reported failures in standard fires to predict structural behavior for design scenarios. The methods illustrated could be used to address the shortcomings of the current simplified conversions of equivalent fire resistance from standard fire tested assemblies.

The remainder of this thesis consists of five chapters. Chapter 2 discusses the previous research leading up to this work. Chapter 3 presents the modeling validation for a pair of structural fire tests to the E119 fire conducted to runaway failure. Included is a detailed breakdown of the thermal and structural modeling strategies and assumptions, as well as comparisons to experimentally recorded data. Chapter 4 introduces the realistic fire modeling concept, and again validates thermal and structural models to experimental data. Chapter 5 conducts a resiliency study analyzing the test specimen parametrically to various fire curves and levels of protection. The survivability of the structure is highlighted and areas where

current practice falls short are demonstrated. Lastly, Chapter 6 concludes this thesis, summarizing the final outcomes of the studies, and discusses future work to be performed.

2.0 Background

Previous studies have demonstrated good agreement between numerical modeling approaches and experimental tests of composite floor beams with shear connections under fire using a variety of approaches. Several studies have used a combination of shell and solid finite elements [19,20] for an in-depth examination of not only the beam but also the shear connection when a one-way spanning composite assembly is subjected to heat-induced weakening and restraint of thermal expansion. These models contribute valuable understanding of the damage sustained by composite floors; however, they have significant computational cost and are not conducive to design practice. Also, these studies focused primarily on the response of unprotected assemblies with a variety of thermal exposures. To meet the need for design-basis tools, several studies, among them [21,22] have validated analytical fiber-based predictions of composite floor behavior which can capture a variety of limit states. These studies generally focused on experimental tests which demonstrated plastic flexural behavior with little local or global instability due to either the size of the specimen or the degree of restraint. The composite decking and reinforcement were also not typical of North American construction. For practical implementation, simple yet conservative models are advantageous, and this study therefore aims at validating models that would be increasingly accessible to structural engineers in practice.

Several studies have expanded past the one-way spanning assumption to model composite floor systems as part of a 3D system for the purposes of model validation [23,24]

or parametric study of prototype composite floor systems with regular [25] or irregular [26] framing layouts. These studies typically utilize shell elements for the slab and fiber-beam elements for the steel beams in order to demonstrate the contributions of the slab's two-way action on the fire resistance of the beam. The objective in most of these studies has been to demonstrate potential enhancements in fire resistance offered by the membrane response of the slab, to the point that passive fire protection could be reduced or eliminated from the secondary floor beams. As a result, the mechanics of the slab's membrane contribution have been examined in-depth [27,28], and several simplified calculation approaches to account for the slab's two-way contribution have been proposed [29,30]. The full-scale Cardington tests mentioned earlier [8,9] have demonstrated the ability of two-way slab action to enhance the resistance of unprotected composite floor beams to realistic fires. Bailey discussed the slab behavior when steel perimeter beams are protected and interior beams are unprotected [29]. The paper established a new design method that accounts for the membrane action in the slab and beam system together, and emphasizes the slab's significant role in the composite floor beam analysis. Bailey's goal was to protect the required beams, and leave the rest unprotected in order to reduce weight and construction time and in turn, construction costs.

Lamont enhanced this idea by performing a case study to show a design approach to engineer the fire protection on the secondary framing beams in an 11-story office building [26]. The E119 standard fire curve was used along with two parametric fire curves with varying ventilation assumptions to capture secondary beam behavior when edge beams are protected or unprotected, and the fire protection in the building was designed according to this behavior. It was concluded that fire protection on some secondary beams

was redundant, and proposed a strategic design method of protecting only specific members. This was a valuable conclusion, but was advised to be conducted on a case-by-case basis which involves a large computational effort.

Though the slab response offers the potential for increased structural efficiency and value engineering to reduce passive fire protection, both experimental [31] and numerical [32] studies have noted limitations of the two-way slab contribution that need further exploration before being accounted for in widespread practice. These items include the need for adequate stiffness in perimeter framing supporting the secondary beams, the need for square or nearly square aspect ratios of composite floor bays, slab detailing needed to resist increased membrane stresses at larger deflection, and steel connection detailing to withstand larger reaction forces and rotations. The evaluation of composite floor systems as one-way spanning elements remains an appropriately conservative approach [33] for introducing performance-based structural-fire analysis to the current prescriptive design environment for composite floors in steel buildings.

Various composite assemblies have been tested under standard and natural fire loading [34,35], but these specimens used a slab on a flat steel deck instead of the corrugated deck customary in current U.S. practice. 3D finite element models were created to investigate the behavior of unprotected composite slim floor beams exposed to various fire curves [36]. The models were validated by comparison to test data and results were tabulated to evaluate degree of damage as a function of fire curve. The detailed computational analysis results indicated that the unprotected steel was able to withstand natural fire curves in all cases studied. For a design engineer, full finite element models are often impractical. This paper aims to determine the modeling resolution warranted for

various fire analyses which would be considered in practice. The modeling used in this study implements SAFIR 2016 [37] which performs uncoupled analyses of a thermal model of each member exposed to fire followed by a structural model. 2D fiber-beam and 3D shell structural models that capably demonstrate composite behavior were created, analyzed, and compared to test findings, thus shedding new light on the readiness of performance-based approaches for structural fire design.

A key aspect of modeling composite floor assemblies is the appropriate representation of the beam-to-slab interface, achieved using cast-in headed studs. Wang et al. [22] provided a numerical validation of two experimental tests conducted with a flat concrete deck that only differed in their percent composite ratios [34]. The models included temperature dependent material properties and consideration of the shear-slip behavior of the shear connectors. Modeling results showed good agreement with test data and confirmed that the 50% composite specimen exhibited a similar failure time as the fully composite specimen despite larger slip. Essentially, the specimens became increasingly composite since the steel beam experienced a more rapid rise in temperature than the slab or shear studs. Fischer and Varma [20] showed that assuming full composite action led to conservative midspan deflection predictions under several fire scenarios. Modeling by Mirza and Uy [38] indicated that composite beams with solid flat slab configurations experience increased shear demand and deformation in the stud connectors, whereas composite beams with profiled slabs on corrugated decks are able to develop the full compressive capacity of the concrete and demonstrate greater structural resistance to fire loading. Further testing on short-span specimens with low composite action [31] and long-span specimens with higher composite action [39] also showed no noticeable shear stud

damage. Collectively, these observations suggest that design-basis models of composite assemblies with corrugated decks (which is typical North American practice) can appropriately capture their fire-induced response by utilizing a simplified "rigid" assumption of the shear interface between the slab and beam. The validity of this assumption will be demonstrated in the analyses presented in this paper.

The modeling considerations for structural-fire engineering consists of three parts, all of which can be of varying complexity. Initially, a fire model must be chosen to capture the energy to be imparted on the structural system from the fire. One on end of the spectrum, simple, standard fires [2,3] with no extinguishing may be chosen as generally conservative but not necessarily representative analysis tools. In the middle ground, fuel loads and compartment parameters can be specified to create a realistic fire curve based on uniform heating assumptions and calibrated equations [13] or one- or two-zone models, as used in the software OZone [40]. Outside the scope of the work considered here, computational fluid dynamics calculations may also be performed to capture the full fire effects. Second, once the fire itself has been described, a heat transfer model must be assumed. This can be done by performing simple lumped mass calculations (using only a few lumped masses) and the laws of conservation of energy or a full finite-element multi-dimensional heat flow analysis can be performed. This paper considers one-dimensional lumped mass heat transfer in the steel and one and two-dimensional heat flow in the slab. The edge of the exposed material is assumed to be equal to the fire temperature, neglecting the three-dimensional ventilation effects. Lastly, the structural model must be defined. As for all other loading, simple beam calculations or complex shell finite element methods can be utilized. For composite floors, the steel experiences three-sided heating causing a

thermal gradient to dramatically affect section behavior. With this in mind, simple beam calculations are not performed due to their inability to capture the mechanics involved. The simplest structural model considered here is a fiber-beam model which allows for temperature-dependent material properties to vary within a single cross section.

3.0 Standard Fire Models

In current practice, prescriptive requirements are used to select passive fire protection according to the building code [1]. Passive protection is selected from tables which are based on "standard" fire tests [2,3]. The standard fires are meant to be conservative, and include a rapid heat increase phase with no temperature decay. Since most fire test data has been acquired for assemblies subjected to standard fire curves, the initial modeling comparisons involve beams tested to ASTM E119.

3.1 Comparison Tests Summary

Two one-way spanning composite beam specimens (loaded to 35% of their ambient factored nominal moment capacity) were subjected to the ASTM E119 standard fire curve [2] using a modular structural testing furnace until the onset of flexural failure. Full details of the specimen design, experimental setup, and test results are provided in Kordosky [18], – a brief summary is provided here. The two structurally identical composite floor beam specimens were constructed using a W12x26 beam with a yield strength of 345 MPa (50 ksi) at a span of 3.34-m (10-ft 11½-in). The beam supported a 142-cm (56-in) wide lightweight concrete (LWC) slab with density of 1938 kg/m^3 (121 pcf) and an 82.6-mm (3.25-in) thickness on top of a 50.8-mm (2-in) profiled metal deck.

The slab was designed with 27.6 MPa (4 ksi) nominal compressive strength (cylinders broken on each test day showed only ~5% increase beyond nominal) and was reinforced with 6x6 4GA welded wire reinforcement (WWR) placed 19.05-mm (3/4-in) below the top of the slab. The composite beam is designed to be partially composite using ten 19.05-mm (3/4-in) diameter, 101.6-mm (4-in) long shear studs that are spaced at 304.8-mm (1-ft) intervals within each flute in the corrugated deck. Based on AISC specifications [14], the specimens were calculated to be 23.6% composite at ambient temperature based on the nominal properties of the concrete slab, steel beam, and the shear studs. The ambient calculations can be found in Appendix 1. The beam was perpendicularly connected to the web of a C15x40 channel (which provided transverse vertical support to the slab) at each end with a shear tab connection with three 19.05-mm (3/4-in) bolts. The outside face of the channel web was bolted to the interior flange face of two W10x26 columns, which provided vertical support and partial restraint of thermal expansion. A schematic of the test setup is provided in **Fig. 3-1**. The applied load in the test was such that the self-weight of the specimen (3.27 kN/m [224 plf]) plus the hydraulic jack load (a total of 158 kN [35.5 kips], with 79 kN [17.75 kips] assumed to be evenly applied at each skid) pushed the beam to 35% of the its factored nominal moment capacity (calculated as $\emptyset M_n$ = 266.1 kN-m [196.3 kip-ft], where $\emptyset$=0.9 [14,41]).

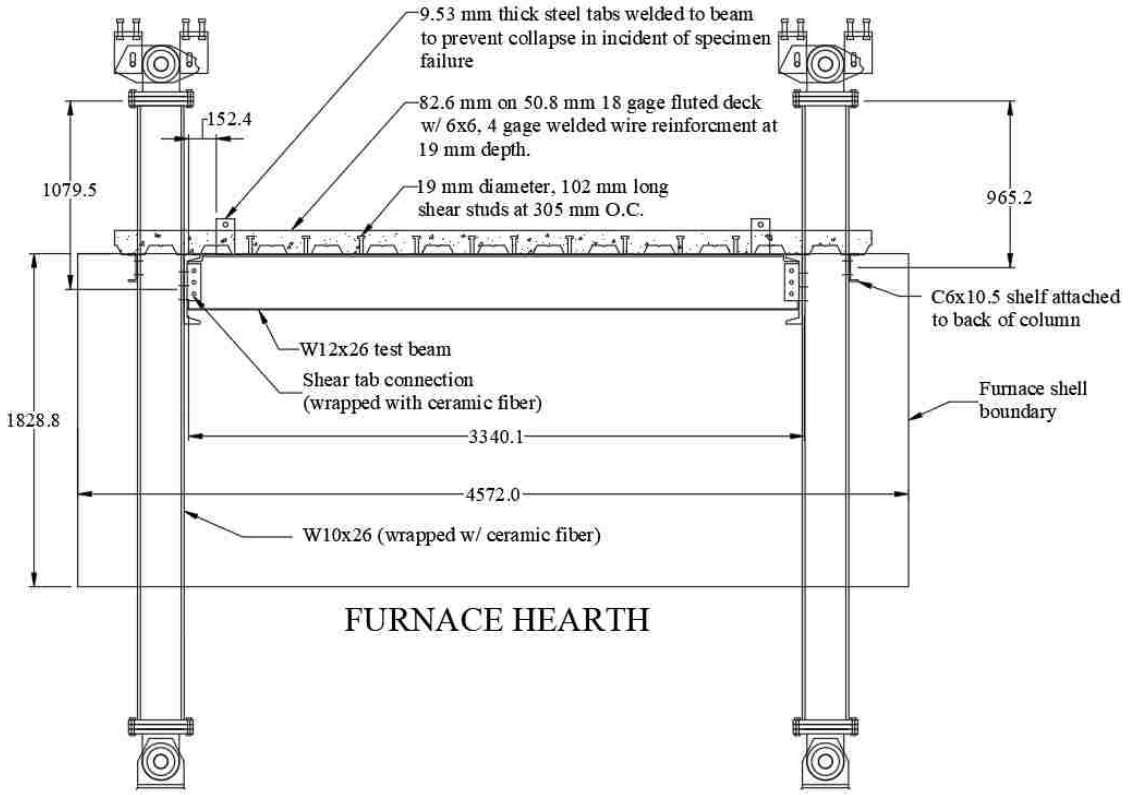

Fig. 3-1. Test specimen and furnace elevation view (units in mm with US framing sizes).

One specimen was protected with SFRM in accordance with the 2014 UL Design No. D902 [42], which is commonly used in current steel building practice. The calculation of SFRM thickness is shown in Appendix 2. An average thickness of 22.2-mm (7/8-in) of CAFCO 300 [43] was applied to achieve a 2-hr rating for both a restrained assembly and unrestrained beam per Section 6C of the D902 design [42] and the SFRM thickness conversion equations provided in ASCE 29-05 [5] – no SFRM was applied to the underside of the corrugated deck in accordance with the D902 design. Several layers of ceramic wool blankets were used to wrap the transverse channels and the W10x26 support columns to mitigate their temperature increase during the fire test. The average steel temperature in the columns reached ~600°C and ~250°C in the protected and unprotected tests,

respectively, due to the ~100-min difference in test duration. A single wrap of ceramic wool blankets was also applied to the shear tab connection zone and extended roughly 355-mm (14-in) from the end of the beam to simulate the typical overshoot of column protection and mitigate the increase of connection temperature.

3.2 Thermal Modeling

Thermal analyses of the steel beam and composite slab are performed separately for simplicity. The thin steel deck is neglected in the analyses. Though a more complex approach could be used, the objective of this thesis is to demonstrate methods conducive to a design scenario. Connection and column temperature test data is explicitly used as thermal input to the corresponding parts in the structural models.

3.2.1 Steel Thermal Profile

Heat transfer on a fundamental basis consists of convection, conduction, and radiation. A simplified method for estimating the temperature of steel framework was created by Quiel and Garlock [44]. The steel beam is assumed to be heated on three sides (relevant for perimeter columns or composite floor beams topped with a slab). A convective heat transfer coefficient of 25 W/(m^2-K) was used. As the standard fires experienced no cooling phase, the convective heat transfer coefficient was constant for the full analysis. MATLAB [45] was used to apply the equations of this method and calculate the temperature of the beam in three-lumped mass sections (the two flanges and web). The bottom flange and web are assumed to be fully exposed to fire. The top flange was modeled

as 75% exposed to convective heat transfer from the fire to account for realistic contact and partial shielding from the bottom of the corrugated deck.

Additionally, reference thermal text files utilizing explicit test temperatures were created. The test recorded bottom flange, web, and top flange temperatures. Using MATLAB, the data was converted into a text file for the structural analysis to reference directly for temperature-dependent material properties.

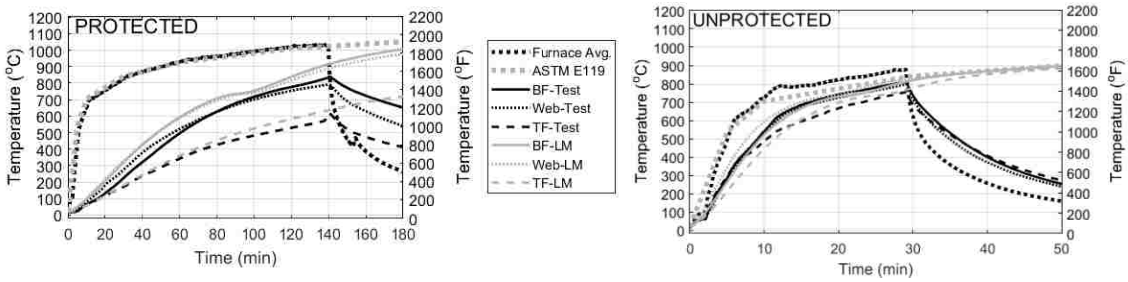

(a) (b)

Fig. 3-2. Beam temperature comparison for (a) protected and (b) unprotected test

Fig. 3-2 plots a comparison between the lumped mass predictions of steel temperature and the test data, which represents the average time history for the flanges and web among the three longitudinal measurement locations [18]. For the protected test (**Fig. 3-2**a), the lumped mass predictions show conservative agreement with the test data for all three plates. Potential causes of the slight overestimation (particularly for the bottom flange and web) include realistic variation in SFRM thickness versus the specified design value, slight deviation of as-tested SFRM thermal properties from the published information [46], the assumptions of a linear thermal gradient through the SFRM layer, and the assumption that the outside edge of the fire protection is equal to the furnace temperature. For the unprotected test (**Fig. 3-2**b), the lumped mass approach shows very close agreement with the average temperature time histories that were recorded during the test. Time history plots

of the heat transferred from the top flange to the slab, q_c, in **Fig. 3-3** show that the protected and unprotected lumped mass calculations develop similar trends and maximum values of q_c, just at different time rates. Not only does the lumped mass calculation require minimal computing power when compared to finite element software, but it can also be more easily modified to account for changes in the contact between the top flange and the slab due to changes in deck profile.

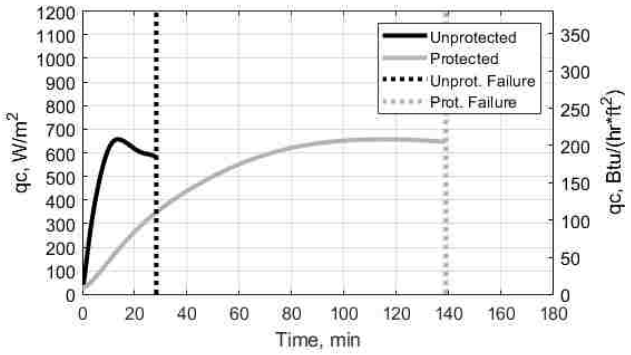

Fig. 3-3. Heat flux from the top flange to slab per [47] and Eq. 4

3.2.2 Slab Thermal Profile

The composite slab will realistically develop a thermal gradient through its thickness, and the slab material is continuous rather than the wide flange which is favorable for sectioning. Lumped mass methods are therefore not an appropriate simplified tool to predict a slab's fire-induced temperature increase. Instead, a simple one-dimensional heat transfer analysis is performed for both the minimum 82.55-mm (3.25-in) and maximum 133.35-mm (5.25-in) thicknesses of the corrugated slab, shown in **Fig. 3-4**a) and c), to obtain an average temperature gradient through its structural (i.e. minimum) thickness. For comparison, a two-dimensional finite element analysis section of the slab, shown in **Fig.**

3-4b), with the corrugated ribs included was created using GiD 13.0.3 [48] and thermally analyzed in SAFIR 2016 [37]. Temperature dependent properties for siliceous concrete are taken according to Eurocode 2 [49] and assume the midrange value for thermal conductivity according to that standard. The ASTM E119 standard fire curve is applied to heat the bottom of the slab in all three models, with the convective coefficient on the heated surface h_f = 25 W/m^2-K and emissivity ε = 0.7 [49]. The top surface of the slab was exposed to ambient conditions of 20°C with h_a = 4 W/m^2-K, consistent with concrete cured via a curing blanket and plastic sheet [50]. The vertical edges shown in **Fig. 3-4** are modeled as adiabatic. Both simple models were discretized in equal layers with 13.75-mm (0.55-in) thickness, and the corrugated model was auto-meshed into fibers with the same maximum edge dimension in GiD 13.0.3. Preliminary analyses showed that these levels of discretization were adequately small to capture the thermal gradient through the slab thickness.

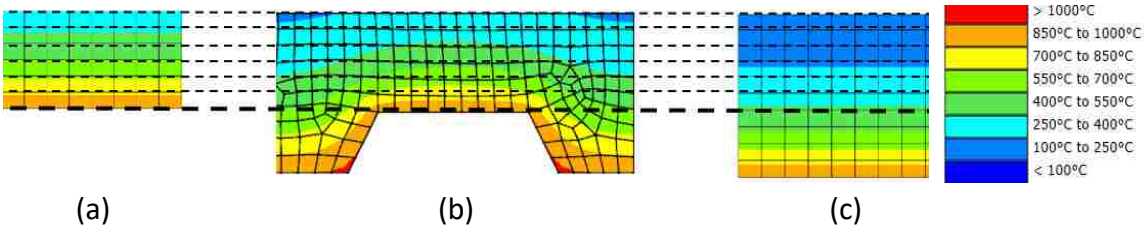

Fig. 3-4. Slab temperatures at runaway failure time of the protected test specimen (138-min) for exposure to the ASTM E119 standard fire: (a) minimum, (b) realistic, and (c) maximum thicknesses.

Two sets of temperature-time histories at each of the equally spaced dashed lines in **Fig. 3-4** were calculated: an average of the two 1D models, and an average of all nodes across the width of the realistic 2D model. In **Fig. 3-5**, the flat slab average shows good agreement with the 2D model. Near 80-min into the E119 fire duration, the flat average

predictions become slightly lower. The prediction could potentially be improved by weighting the temperatures obtained in the minimum thickness 1D model and considering top flange heat transfer. For the purpose of this study, the average 1D temperatures will be used in all simplified structural analyses to evaluate their effect on capturing the experimental flexural behavior of these specimens from a simplified, design-focused perspective The average thru-thickness temperatures from the more realistic 2D model will be used in structural models with greater complexity, with the goal of precisely representing test performance.

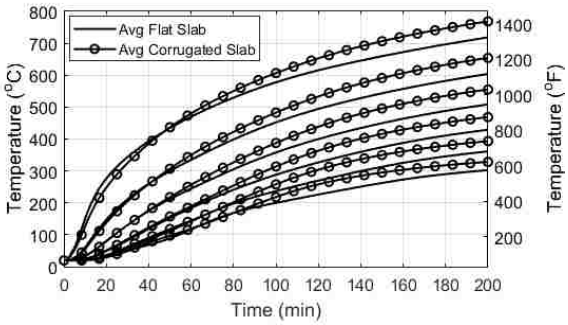

Fig. 3-5. Comparison of slab model temperatures at the thru-thickness locations.

In **Fig. 3-6**, the temperature-time histories from the 1D and 2D slab thermal modeling approaches at the top unexposed face of the slab are compared to test measurements for the protected and unprotected test. The protected test data shows closest agreement with the 1D model of the 133.35-mm (5.25-in) maximum slab thickness. During that test, water escaping the heated concrete began to collect and vaporize at the top slab surface. The thermocouples came into contact with this water, which can be observed by the plateau in **Fig. 3-6**(a) of measured temperature at 100°C (i.e. water's boiling point) from the 50- to 100-min mark. Due to the water interference, the comparison of numerical and experimental data is less reliable **Fig. 3-6**(b) shows similar agreement between the

models and test data for the unprotected test as shown over the first 30 minutes of the protected test. The protected test ran for a longer period of time, allowing the slab to absorb more heat and thus reach a higher temperature than the shorter, unprotected test. The unprotected test did record bottom of deck data, but comparison is not feasible based on the rough modeling conducted here. The thermocouples were placed on the bottom of the steel deck, which is more conductive than the slab itself, and the slab edge in thermal models is assumed to be the exact temperature of the fire. The test results fall between fire temperature and the averaged flat slab temperature bottom fiber temperature, but a comparison is not meaningful. Temperatures were not measured through the slab thickness during the experimental tests, and a comparison of temperatures through the slab thickness is also therefore not possible.

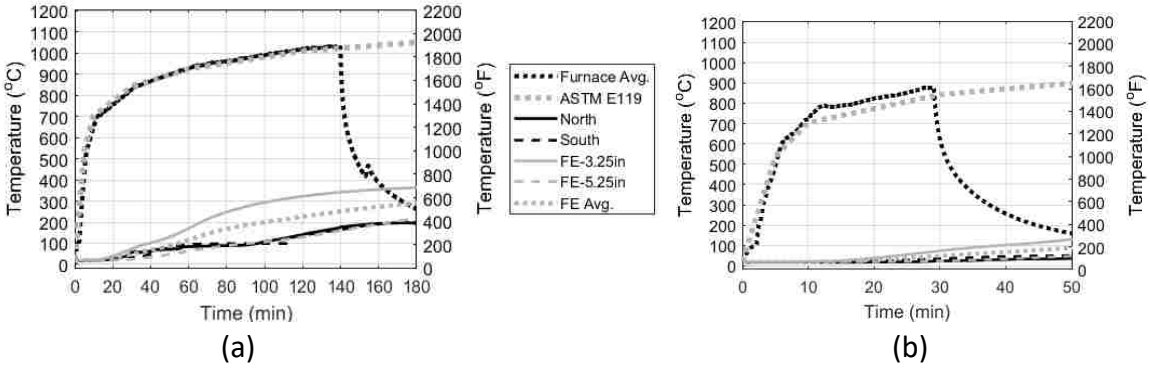

Fig. 3-6. Top of slab temperature comparison for the (a) protected and (b) unprotected test

3.3 Structural Modeling

As shown in **Fig. 3-7**, two types of structural models were created in SAFIR 2016 [37] with different levels of complexity. In the "complex" option, the composite beam and slab are composed of 3D shell elements, and the shear tab connection and shear studs are explicitly represented at their tested locations. This model is used to obtain a more precise

prediction of the tested specimen behavior, particularly to allow the emergence of potential local or global instability. In the "simple" option, the composite beam and slab are modeled as a single fiber-beam cross-section, thereby assuming full composite action between the two. The creation and use of this model is far more accessible to practicing engineers. Though the 2D fiber-beam model cannot explicitly consider stability limit states, the potential for local buckling is checked at every time step using an effective stress approach proposed by the SAFIR developers [51], and the potential for lateral torsional buckling can be evaluated per Vila Real et al. [52]. Note that **Fig. 3-7** is shown with symmetry for brevity – both models are analyzed using the full assembly (i.e. with the full span and both support columns) to avoid the complication of symmetric boundary conditions (especially for the 3D shell model). Temperature dependent structural properties for hot-rolled steel, siliceous concrete, and steel reinforcement are taken according to Eurocode [13,49]. Nominal values for steel yield strength and concrete compressive strength are implemented, and tensile concrete strength is conservatively neglected.

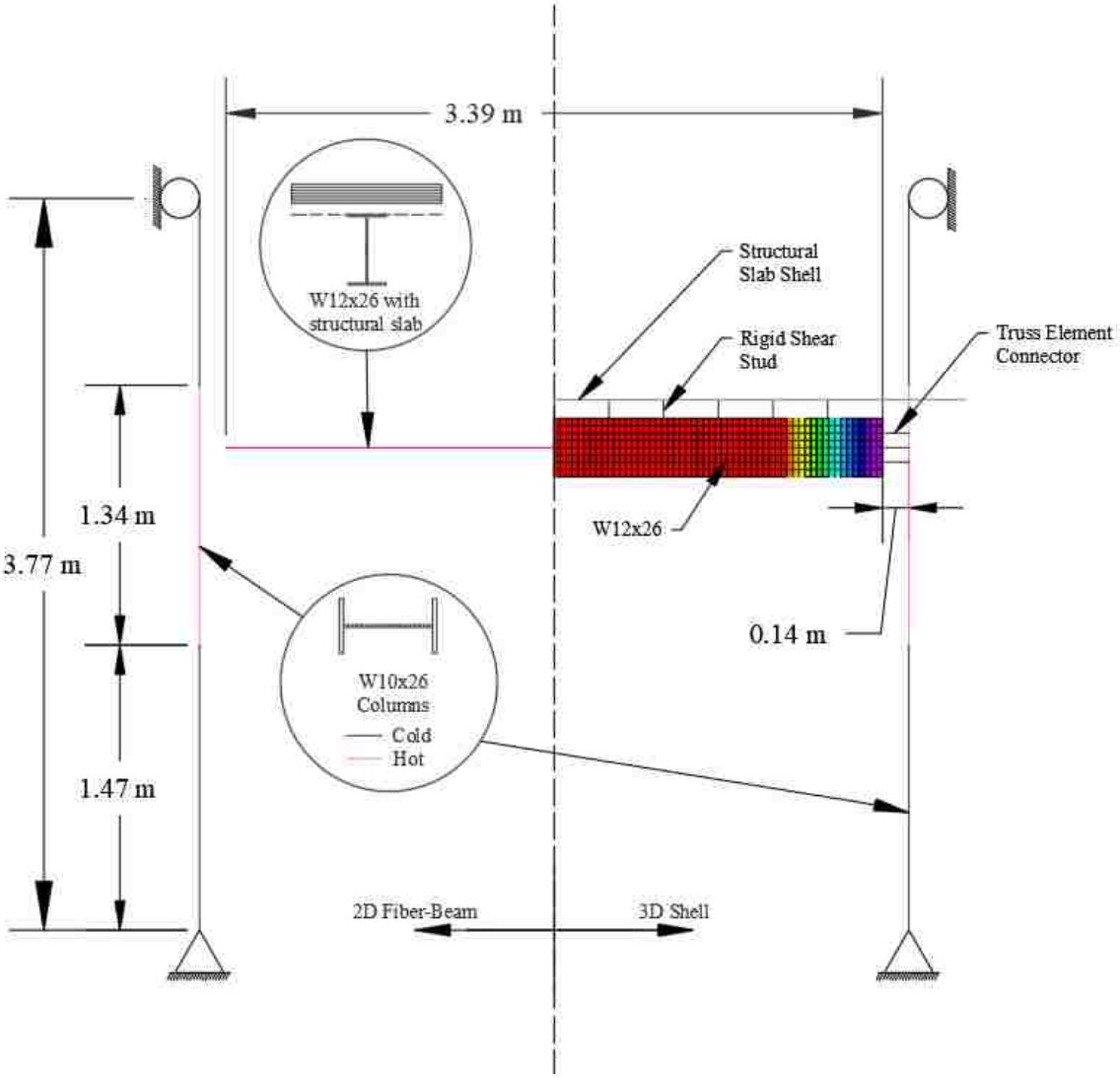

Fig. 3-7. Structural modeling options: 2D fiber-beam and 3D shell

In both model types, the support columns were modeled using fiber-beam elements with 22 strip fibers over the cross-sectional depth (one in each flange and the rest in the web) and 14 element discretization along its 3.767 m (12-ft 4¼-in.) length. The ends of each support column were connected to the heavy reaction frame using large clevis connections [18] to enable a true pinned end with no bending moment. The modeled length of the column was taken as the centerline distance between the shear pins in each clevis. The top clevis has vertically slotted holes and is therefore modeled as a vertical roller. **Fig.**

3-7 shows that the column length within the furnace is heated while the lengths outside the furnace are approximated as remaining at ambient temperature. Though covered with ceramic fiber blankets during the tests, the column section within the furnace experienced a relatively uniform temperature increase. The average column temperature-time history obtained from the test results is assigned uniformly to all fibers to avoid performing thermal analysis for these elements.

The self-weight of all components is directly applied to each discretized shell or fiber-beam element per its material properties. Though not explicitly modeled in either the 3D shell or 2D fiber-beam model, the weight of the perpendicular slab ribs is applied as an additional smeared load to the slab finite elements. The two loads applied at the third-points along the beam span via the hydraulic jack and steel-framed loading tree in the experimental tests are applied as point loads at the same locations to the top of the slab and held constant throughout the simulation. Dynamic analysis with zero damping (negligible due to the low velocity response of the specimen) is performed using a Newton-Raphson numerical solver to achieve convergence. A comeback routine is used to allow the simulation to continually half the time step (to a limit of 0.0001 seconds) until convergence is reached; thus enabling the analysis to cope with a high degree of nonlinear response.

3.3.1 Composite Action

It has been shown that composite beams act increasingly composite through the duration of fire tests, as the beam heats up faster than the slab, and that assuming full composite action throughout leads to conservative predictions of midspan deflection [20,22,31,34]. A time history of the beam's percentage of composite action over the

duration of each test was estimated by leveraging the beam and slab temperatures from the simplified models to obtain temperature-dependent material properties at every time step and recalculate the composite percentage over time per AISC 360-16 [14]. The steel temperature was calculated as a weighted average of the lumped mass results. The average temperature in the minimum structural thickness of the slab was calculated using the average results of the two simplified 1D models. The shear stud temperature was calculated as an average of slab temperature and steel top flange temperature, which is consistent with observations reported by Selden [53] from other fire tests on composite floor systems where stud temperature was monitored. **Fig. 3-8** shows that the unprotected assembly reaches full composite action after approximately 25 minutes, and the protected assembly reaches full composite action near 133 minutes. The rise in composite action can be attributed to the fact that the steel temperature increases faster than concrete. The fully composite assumption is implemented in all structural models, and its viability is demonstrated via comparison to experimental results.

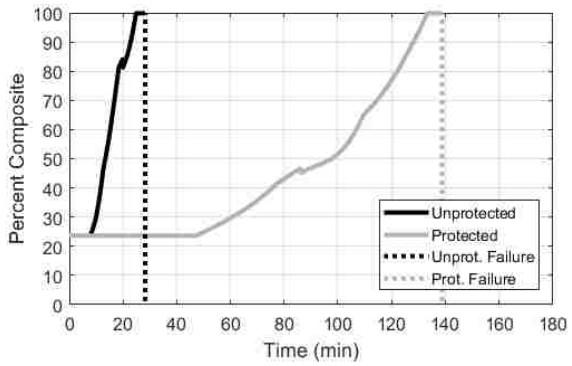

Fig. 3-8. Time histories of the composite percentage in the protected and unprotected test assemblies.

3.3.2 Three-Dimensional Shell

Fig. 3-9 shows the full assembly of the 3D shell model, in which the flanges and web of the steel beam were modeled with 4-noded shell elements discretized to a 38.1-mm (1.5-in) maximum edge dimension. The slab shell elements were modeled with a 282-mm (11.1-in) maximum edge dimension and constant thickness of 82.55-mm (3.25-in) corresponding to the minimum structural thickness (neglecting the contribution from the ribs). The steel mesh in the slab is represented as uncoupled smeared layers with equivalent area per width in both the longitudinal and transverse directions. The equivalent reinforcement area in the longitudinal direction matched the WWR in the tested specimens, while that in the transverse direction was increased slightly to account for the flexural contributions of the perpendicular ribs (which were not modeled). Preliminary analyses confirmed that these levels of discretization were sufficient to not influence the modeling results. All shell layers are located at their thickness centerlines per the specimen geometry. The transverse channel at the beam ends is included to provide transverse support to the slab per the tested assembly. This element was wrapped in several layers of ceramic blankets during the test and did not experience a severe enough temperature increase to cause significant stiffness loss. This element is therefore modeled at ambient temperature.

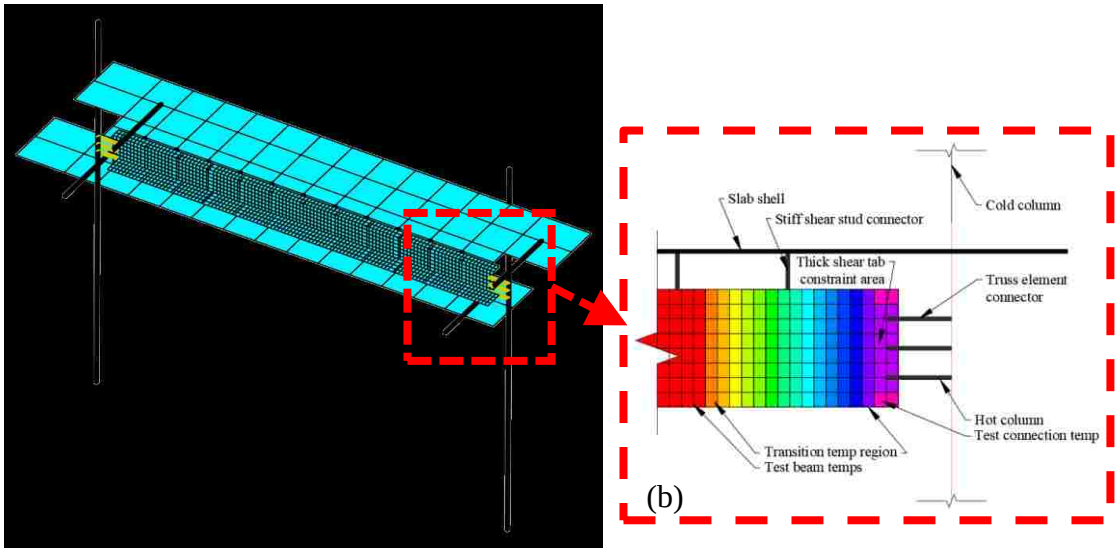

Fig. 3-9. SAFIR shell model: (a) isometric view and (b) connection region

Imperfections were added to the geometry of the beam web and bottom flange via bidirectional sinusoidal patterns to promote the emergence of potential local buckling. The top flange received no imperfections because it is braced against the metal deck and is therefore unlikely to experience local buckling. The amplitude of the imperfections in the web was assigned a value of *d/500* (calculated to be 0.5-mm), where *d* is the height of the web plate. Seven sinusoidal wavelengths were imposed along the full length of the web per previous research by Quiel and Garlock [54]. A single half wavelength (with maximum amplitude at mid-height) was imposed over the web depth. The imperfections in the bottom flange (with a maximum amplitude of 0.312-mm) were imposed to be geometrically congruent with those in the web (i.e. to preserve their perpendicular interface). To enable the emergence of potential lateral instability, the steel beam was also given an initial out-of-straightness of span/1000 in accordance with Appendix 1 of AISC 2016 [14] for inelastic analysis. This imperfection was applied as a lateral shift via a sinusoidal half-wavelength to the bottom flange, with all other plates maintaining geometric compatibility.

The shear studs spaced at every 304.8-mm (1-ft) were modeled using a connector element composed of a single fiber to simulate composite action between the beam and slab. The structural properties of the connectors were kept at ambient throughout the analysis and given an artificially simple modulus of elasticity of 500 GPa to ensure they would have a "very stiff" shear response. The ends of this element were moment connected to vertically aligned nodes in the slab shell layer and the top flange shell layer. To improve numerical convergence and overcome the effects of localized stress concentration, the row of nodes with the connector contact and the two rows adjacent on the top flange shell layer were assigned the same vertical displacement and rotation about the transverse axis. This approximation reasonably captures the contact of the deck rib with the top face of the flange at a shear stud location, smoothing out the load transfer.

The shear tab connection was modeled as three single-fiber truss elements (i.e. axial forces only), each with stiffness representative of the lateral resistance of the bolts and their interaction with the connection plates. As shown in **Fig. 3-9**, each element connected a node on the web (at the approximate location of the actual bolt hole) to a column node at the same vertical location. The web shells sharing the "bolt hole" nodes were thickened to include the shear tab thickness – this was needed to mitigate the numerical instabilities induced from the stress concentration at these nodes. Since these connectors are axial load-carrying only, vertical displacement constraints were applied to force the tab to maintain the rotation of the channel to support the gravity reactions. The connector elements were assigned a stiffness of 33.3 kN/mm (190 kip/in) per ambient bolt stiffness data for three 19.05-mm (3/4-in) bolts in a shear tab from Peixoto et al. [55]. Previous research has shown that bolt shear capacity at temperatures below 300°F (572°F) is not substantially affected

when compared to ambient capacity, but at 600°C (1112°F), shear capacity drops to 20% of ambient [56]. The unprotected test connection zone remains below 204°C (400°F), while the protected test connection zone exceeds this temperature in the last third of the test, reaching a maximum of about 575°C (1067°F) prior to failure. Preliminary models of the protected test were analyzed with the connection zone truss elements at 20% of their ambient stiffness for the entire test duration to conservatively estimate behavior. The deflection was about 20% higher at the 2-hour mark, with the models being slightly more flexible and failing about 7 minutes earlier than the ambient stiffness models. The ambient stiffness is used as a simplification in the 3D shell analyses presented in this paper and is shown to provide an acceptable prediction of the connection's lateral and rotational restraint of thermal expansion. Damage to the connection plates and bolts using detailed, temperature dependent modeling approaches will be evaluated in future work.

The 3D shell model was analyzed exclusively using steel temperatures from the experimental tests and average minimum slab thickness temperatures from the corrugated thermal model (**Fig. 3-5**) in order to directly evaluate the structural response of the tested specimens. The same thru-thickness temperature profiles were uniformly applied to the entire slab, thus conservatively neglecting the slightly lower temperatures that would realistically occur at the slab's contact with the beam. As shown in **Fig. 3-9**, the average flange and web temperatures were applied over the majority of the beam length except for the 355-mm (14-in) segments on both ends that were covered in ceramic fiber blankets during the test. The average temperature measured at the connection during each test were input into the full section depth (web and both flanges) at the 50.8-mm (2-in) ends of the beam (i.e. the connection zone). The temperature in the web and flange plates over the

remainder of the blanket-covered region was linearly increased from the connection temperature to their corresponding span temperature over the remainder of this transition.

3.3.3 Simplified, Two-Dimensional Fiber-Beam

As shown in the section view in **Fig. 3-7**, the composite section for the 2D fiber-beam representation of the composite beam and slab was divided into 38 strip fibers over its depth: 6 in the slab (to match the thermal model thru-thickness discretization in **Fig. 3-4**), one for each flange, and the rest for the web depth. The cross section is shown in **Fig. 3-10**. The steel welded wire reinforcement is conservatively neglected for simplicity, as the slab ends were unrestrained. Future work will examine the influence of a continuous slab condition beyond the steel beam connection. In those cases, the slab reinforcement will play a more significant role and would be included. The transverse channels were also neglected in the 2D models since out-of-plane behavior of the slab is not significant for this loading scenario.

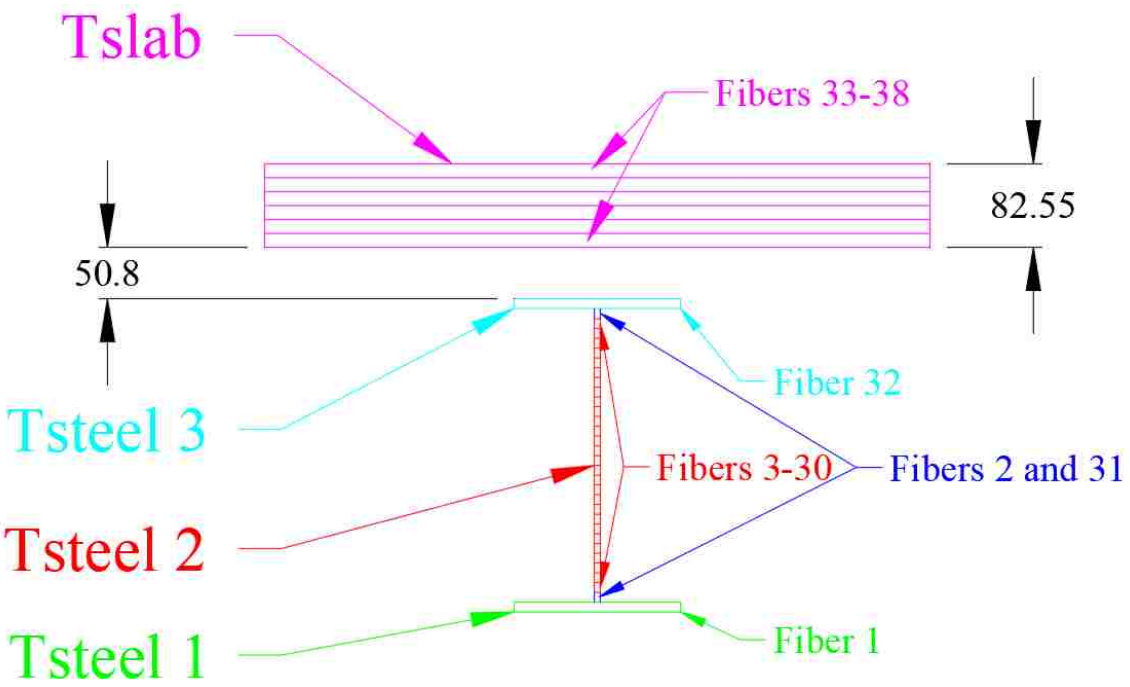

Fig. 3-10. Cross section of W12x26 fiber-beam model (dimensions in mm)

The fiber-beam elements for the composite beam were discretized at approximately 304.8-mm (1-ft) lengths per previous research by Quiel and Garlock [33]. Simulations of the protected and unprotected tests were performed using two constraints between the beam end and the column node at the same vertical location: displacement only (i.e. pinned), and all displacement and rotational degrees of freedom (i.e. fixed). The results of these models would be expected to bound the experimental response, for which the shear tab connections would realistically provide a small yet significant amount of rotational restraint. Future work will explore the structural ramifications of using a simplified rotational spring or component-based connection model [57] for modeling the fire-induced response of these assemblies.

Analyses with the 2D fiber-beam model were made with two sets of thermal input. The first used experimentally measured steel temperatures and slab temperature profiles

obtained from the realistic 2D corrugated model, matching that used for the shell model. The main span steel temperatures were assigned to the full length of the fiber-beam model – the reduced temperatures at the blanketed beams ends and the connection were not considered (since the end elements are approximately the same length as the connection region in the shell model). This thermal approach is intended to evaluate the fiber-beam model's capability to lead to efficiently generated, accurate representations of the experimental data and shell model using the same thermal input. The second set of thermal input, representing a "blind" case conducive for design, implements the lumped mass steel temperatures and the average of the 1D flat slab thermal analyses. The steel was assigned either test temperatures (separated into bottom flange, web, and top flange) or three lumped mass temperatures, depending on the model. The bottom flange temperature was assigned to Fiber 1, the web temperatures to Fibers 3-30, and the top flange temperature to Fiber 32. Fibers 2 and 31 were assigned the average of the web temperature and the adjacent flange temperature to smooth out the temperature transition and improve numerical stability so the stiffness change was less discrete. The breakdown of fiber temperatures is shown in **Fig. 3-10**.

3.4 Model Validation

Plots comparing the experimental and numerical time histories of the beam's vertical midspan deflection and lateral column movement are provided in **Fig. 3-11** and **Fig. 3-12** for the protected and unprotected specimens subjected to the ASTM E119 standard fire. Experimental curves represent the average of North/South and East/West measurements made during the tests [18]. The following notation is used to identify each

composite beam model: element type, end conditions ("S" for shell elements and realistic connection, "BP" and "BF" for fiber-beam with pinned and fixed ends) and thermal input ("TT" for test temperatures of the beam and the detailed slab profile, and "LM" for the lumped mass steel temperatures with the simplified slab profile).

3.3.1 Predictions of Structural Performance

Experimental deflections in **Fig. 3-11** and **Fig. 3-12** show some slight initial discrepancy from the numerical results in ambient deflection under the applied loads and self-weight – this is most likely caused by realistic flexibility and play in the test setup prior to full engagement that is unaccounted for in the models. This discrepancy notwithstanding, the TT models show close agreement with the displacements from both tests, with the more precise shell response bounded by the pinned and fixed fiber-beam models as expected. As the composite beam heats, its thermal expansion is partially restrained by the support column, which as a result is pushed outward (i.e. negative displacement). The model column displacements capture the displacement from thermal expansion well. Future steps could include developing a temperature-dependent spring to represent the lateral and rotational stiffness provided by the columns. The downward midspan deflection of the specimen increases steadily as the beam temperature increases until accelerating as the maximum steel temperature approaches 700°C (1292°F) and the combined cross-section approaches 100% composite (**Fig. 3-8**). As summarized in **Table 3-1**, the TT models demonstrate times to runaway failure that are very close and slightly conservative relative to the experimental results. The protected, pinned model has the largest difference between E119 and runaway failures.

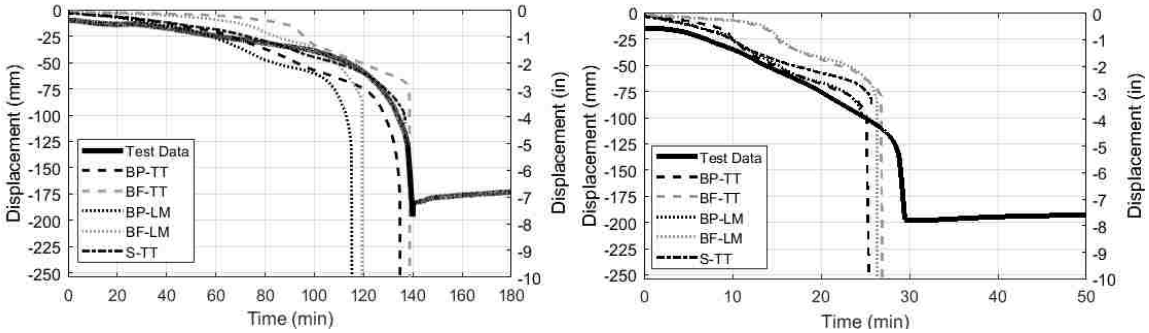

(a) (b)

Fig. 3-11. Beam deflection for (a) protected and (b) unprotected test

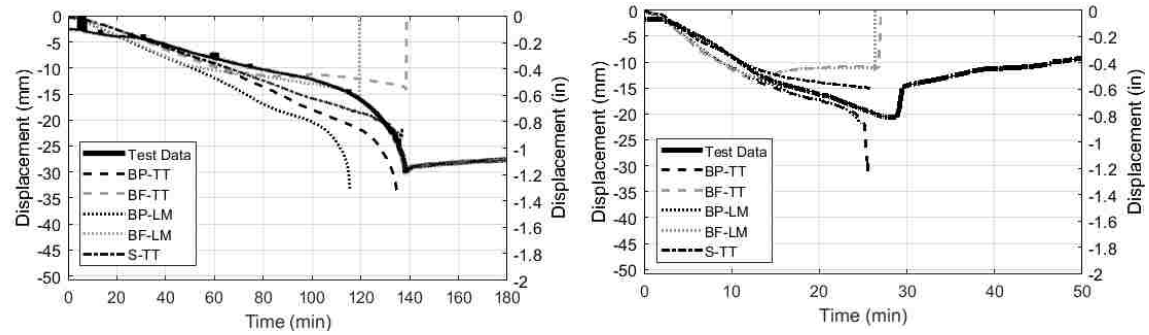

(a) (b)

Fig. 3-12. Column deflection for (a) protected and (b) unprotected test

Table 3-1. Beam failure times (min) by ASTM E119 deflection limits (runaway deflection)

		TT Models			**LM Models**	
Specimen	**Test Result**	*Shell*	*Beam Pinned*	*Beam Fixed*	Beam Pinned	Beam Fixed
Protected	130 (138)	*134 (136)*	*125 (134)*	*138 (138)*	110 (115)	119 (119)
Unprotected	22 (28)	*25 (25)*	*24 (25)*	*26 (27)*	24 (24)	26 (26)

The LM models also demonstrate good agreement with experimental displacements until reaching runaway failure about 10-15% earlier. As shown previously in **Fig. 3-2**, the LM models predicted slightly higher steel temperatures, especially for the bottom flange

and web, relative to those recorded during the test. Improvements in the LM approach would produce even better agreement in failure time; however, the current LM predictions are acceptably conservative to be used as "blind" design-basis calculations.

3.3.2 Modes of Structural Failure

The deflected shapes of both the protected (**Fig. 3-13**) and unprotected (**Fig. 3-14**) 3D shell models at runaway failure are very similar to those observed during testing [18]. The protected beam in **Fig. 3-13** experiences only minor out-of-plane web deformation near the transition to the cooler blanketed connection zone. As a result, the bottom flange remains relatively straight. The unprotected beam in **Fig. 3-14** experiences considerably more web deformation at the same location, leading to a lateral sway of the bottom flange as the beam reached runaway. Real-time observations of the specimens during the test via a high-temperature probe camera revealed that the bottom flange sway in the unprotected specimen did not occur until the final few minutes of the test before failure. Post-test inspections of both specimens indicated that the bottom flange and the face of the support column did not come into contact due to the relatively low support rotations for the tested span as well as the gap between them. The relative displacement between the end of the bottom flange and the column in both 3D shell models also indicated no contact between them.

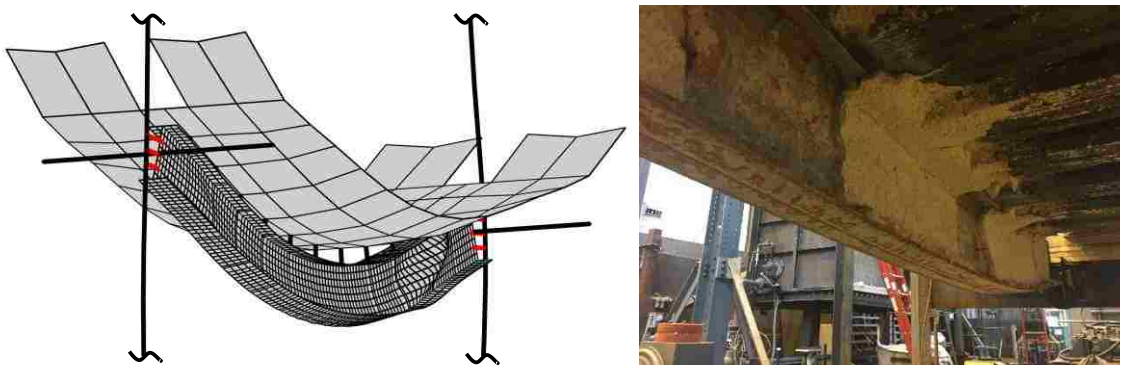

Fig. 3-13. Final deflected shape of the protected specimen: (a) S-TT model at runaway failure (5x magnified), and (b) post-test photo.

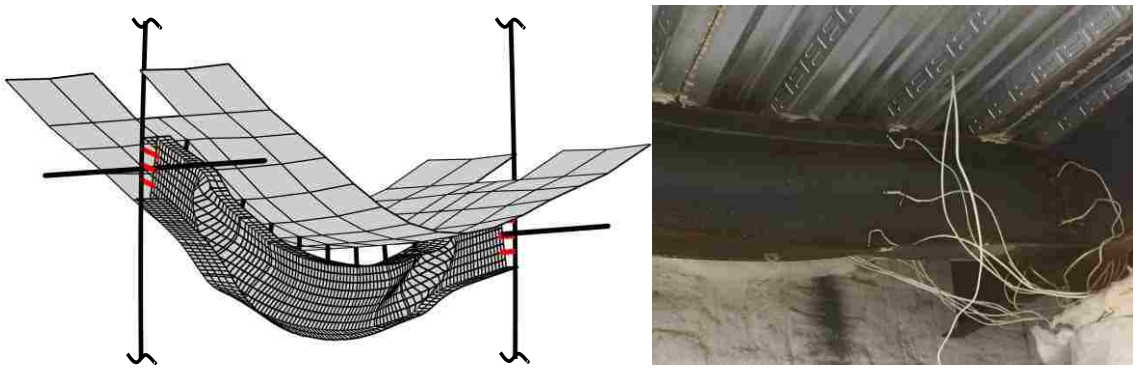

Fig. 3-14. Final deflected shape of the unprotected specimen: (a) S-TT model at runaway failure (5x magnified), and (b) post-test photo.

End reactions from the structural models based on explicit test temperature are presented in **Fig. 3-15** and **Fig. 3-16**, for axial force and bending moment, respectively. The shell model internal forces were extracted from shell stresses at a cross-section approximately 95.25-mm (3.75-in) from the end, instead of directly at the beam end where the flange tips were free and the shear tab shells were thickened. All three models (two fiber-beam and one shell) show the beam end remains in compression for the full duration of the test. The fixed models result in slightly less axial force than pinned or shell. The

shell models had a temperature transition zone which stepped down the thermal profile gradually from test beam temperature to connection zone temperature, so the beam ends in the shell are not in an identical thermal state as the fiber-beam. For the protected test, the beam and connection temperatures are relatively closer, leading to good agreement between the pinned and shell model axial force. The unprotected models in **Fig. 3-15**(b) show a significantly higher axial force in the shell model. The shell section in the connection region is dramatically cooler than the corresponding location in the two-dimensional models, giving the shells at the end of the beam a higher stiffness than the hot fibers and accounting for the increase in axial force. The bending moments at the end show the connection behaves more closely to the pinned model initially, transferring minimal moment to the columns. However, the shell model demonstrates that as the beam heats up, the connection behavior trends towards a fixed connection. The unprotected shell model shown in **Fig. 3-16**(b) transfers a larger bottom flange compressive force as the flange of the beam in the connection region is significantly cooler than the inner test span, leading to a larger hogging moment. The exact rotational restraint provided by heated connections is not the focus of this study, but the shell model shows relatively acceptable behavior for an analysis on plastic beam behavior.

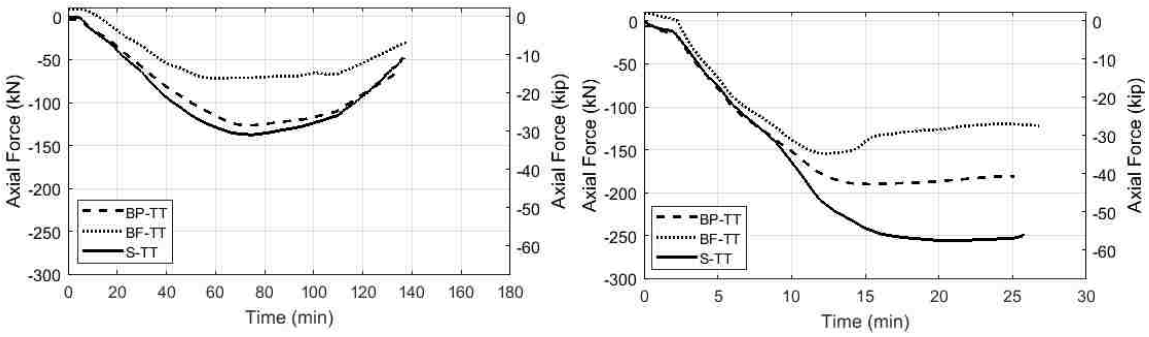

(a) (b)

Fig. 3-15. Axial force (tension = positive) at the beam end for (a) protected and (b) unprotected test.

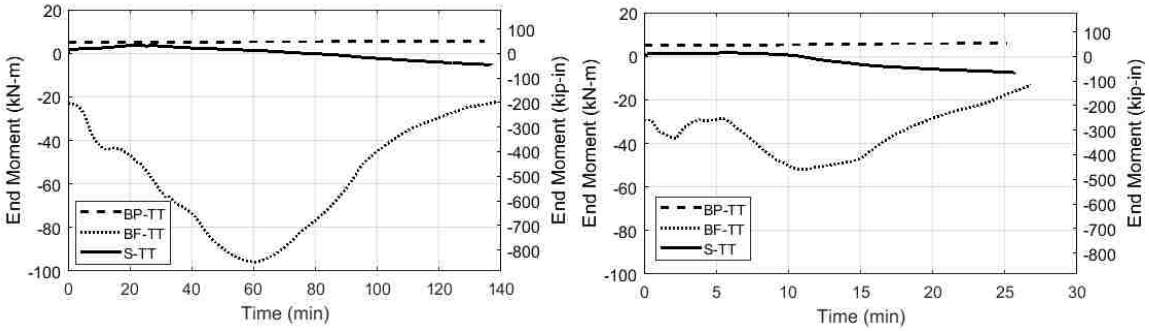

(a) (b)

Fig. 3-16. Bending moment (sagging = positive; hogging = negative) at the beam end for (a) protected and (b) unprotected test.

Despite the connection remaining in compression for the duration of the test, the bottom flange at midspan remains entirely in tension for all three models. This eliminates the possibility of lateral-torsional buckling, which can only occur with the presence of an unbraced compression flange. This confirms the test observation of the beam lateral motion being a result post-plastic sway rather than lateral-torsional buckling. Once again, the shell model shows good agreement with the pinned two-dimensional fiber-beam model. Checks for local and global instability in all fiber-beam models based on stress in the flange and web plates along the length indicated no onset of buckling.

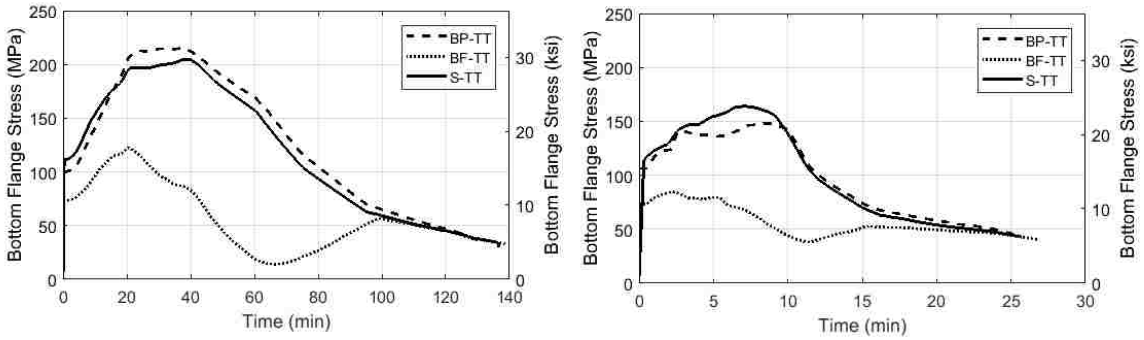

(a) (b)

Fig. 3-17. Midspan stress in bottom flange for (a) protected and (b) unprotected test.

As the beam heats up, the standard axial load-moment (P-M) failure envelope begins to skew due to the shift of the neutral-axis described by Garlock and Quiel [58]. Their research showed that using the original failure envelope to analyze beam-columns under fire is conservative in some scenarios and unconservative in others, and therefore warping of the envelope must be considered on a case-by-case basis.

A step-by-step breakdown of the P-M curve formulation for the protected, pinned beam is presented in **Fig. 3-18**, followed by a summary of the curves generated from the various models considered. It is crucial to note that these diagrams represent the internal forces in the steel alone, not the total net section axial load and moment carried by the composite beam made up of the steel and slab. The positive P value corresponds to tension and the positive M value represents sagging moment about the steel geometric neutral axis. The large open blue circle is the initial P-M load under ambient conditions, while the solid blue dot is the time plotted (listed above the plot). The small markers along the curve represent 5-minute intervals.

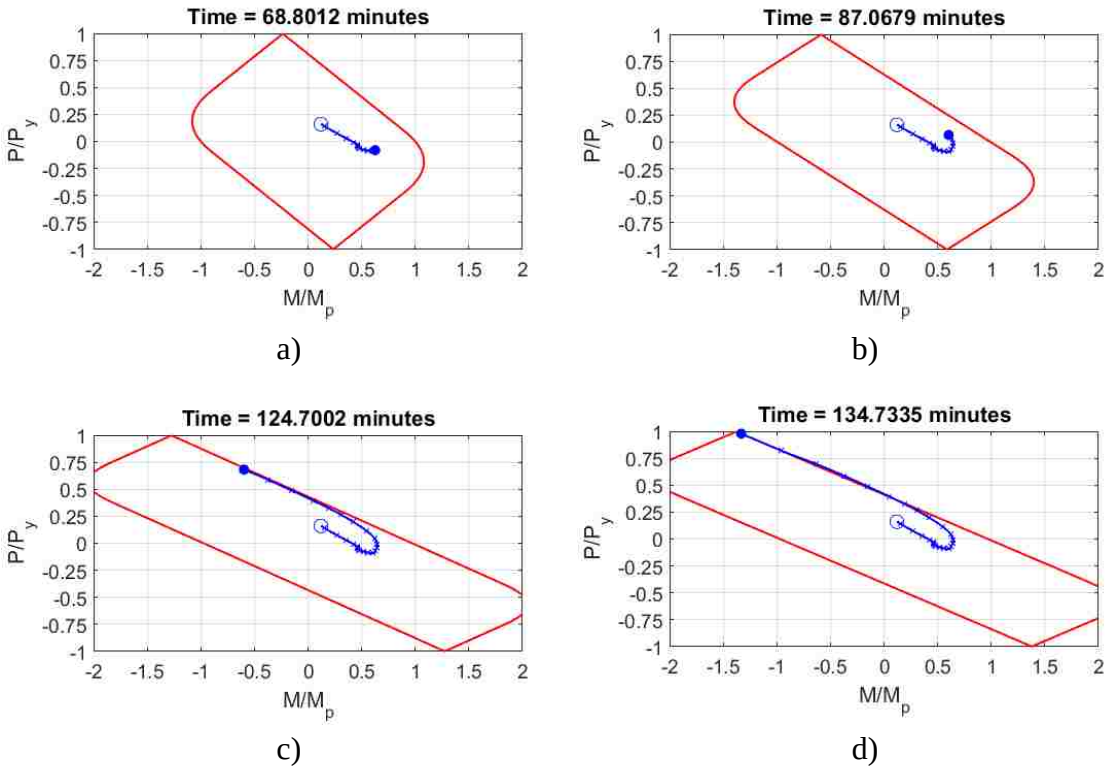

Fig. 3-18. Normalized P-M diagrams for the steel beam at midspan for the BP-TT analysis.

Initially, at the open, starting circle, the steel beam begins with a small tensile load and sagging moment generated by the gravity loading. The concrete is taking compression, leaving the steel in net tension, and the distribution of the forces result in a sagging moment. **Fig. 3-18**a) shows a decrease in axial force and an increase in moment at approximately 68 minutes. As the temperature of steel increases, the steel tries to expand. Since it is restrained from expansion by the column, the beam experiences compressive forces and decreases the net axial load in the steel section. However, due to more compression being present in the steel overall, the tension in the bottom flange continues to increase to carry the moment generated from the unchanged applied mechanical load, creating a larger sagging moment. **Fig. 3-18**b) shows the steel interaction near 87 minutes. The system is behaving

increasingly composite, with both the concrete compression increasing and the steel tension increasing. This action reduces the moment being carried in the steel section alone as global tensile forces increase in the steel as the beam deflects. The moment in the steel begins to reverse direction, as the concrete continues to take additional compression. Simultaneously, as the steel temperature increases, the yield strength decreases leading to the axial load within the beam being a higher percentage of remaining yield strength, hence the movement up the normalized diagram. The cooler top flange takes higher compressive forces to counter the shifting neutral axis, causing the normalized moment about the steel geometric neutral axis to move closer to zero.

As the bottom flange continues to weaken, tensile forces migrate into the top flange, as the bottom flange is not strong enough to carry the full gravity and thermal load. This behavior continues through **Fig. 3-18** c), where the forces contact the warped plastic failure envelope at 124 minutes, more than 10 minutes before runaway collapse was observed. The moment has actually moved into the negative half, representing a hogging moment in the steel due to the entire section being in tension, with larger force resultants above the geometric neutral axis in the cooler top flange. The space between 5-minute marks increases as the curve approached indicating a more rapid change in the normalized internal force state. Lastly, **Fig. 3-18** d) shows the final time step of the analysis, when the model fails, after significant plasticity at midspan. The beam reaches about 25% higher than its ambient plastic moment ratio, and then fails to take any more load as the deflection becomes too large.

The analyses presented used explicit test temperature data as input to the structural model in an effort to compare the structural models to reality when temperatures are known

rather than a variable. However, models run using the lumped mass approach behaved similarly as shown comparing **Fig. 3-19** to **Fig. 3-18** d). The higher lumped mass temperatures lead to a failure time 20 minutes sooner than the test temperatures, but the steel carries the load in the same relative manner.

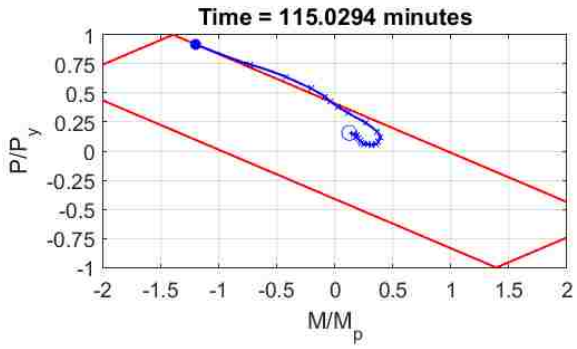

Fig. 3-19. Normalized P-M diagram for the steel beam at midspan for the protected BP-LM analysis at runaway failure.

Fig. 3-20 shows the final axial-moment (P-M) diagrams for the fixed and pinned steel beams at failure. The left figures are for the protected test, and the right figures show the unprotected. The first pair of figures, (a) and (b), represent the pinned beam midspan elements, (c) and (d) the pinned end, (e) and (f) the fixed midspan, and (g) and (h) the fixed end.

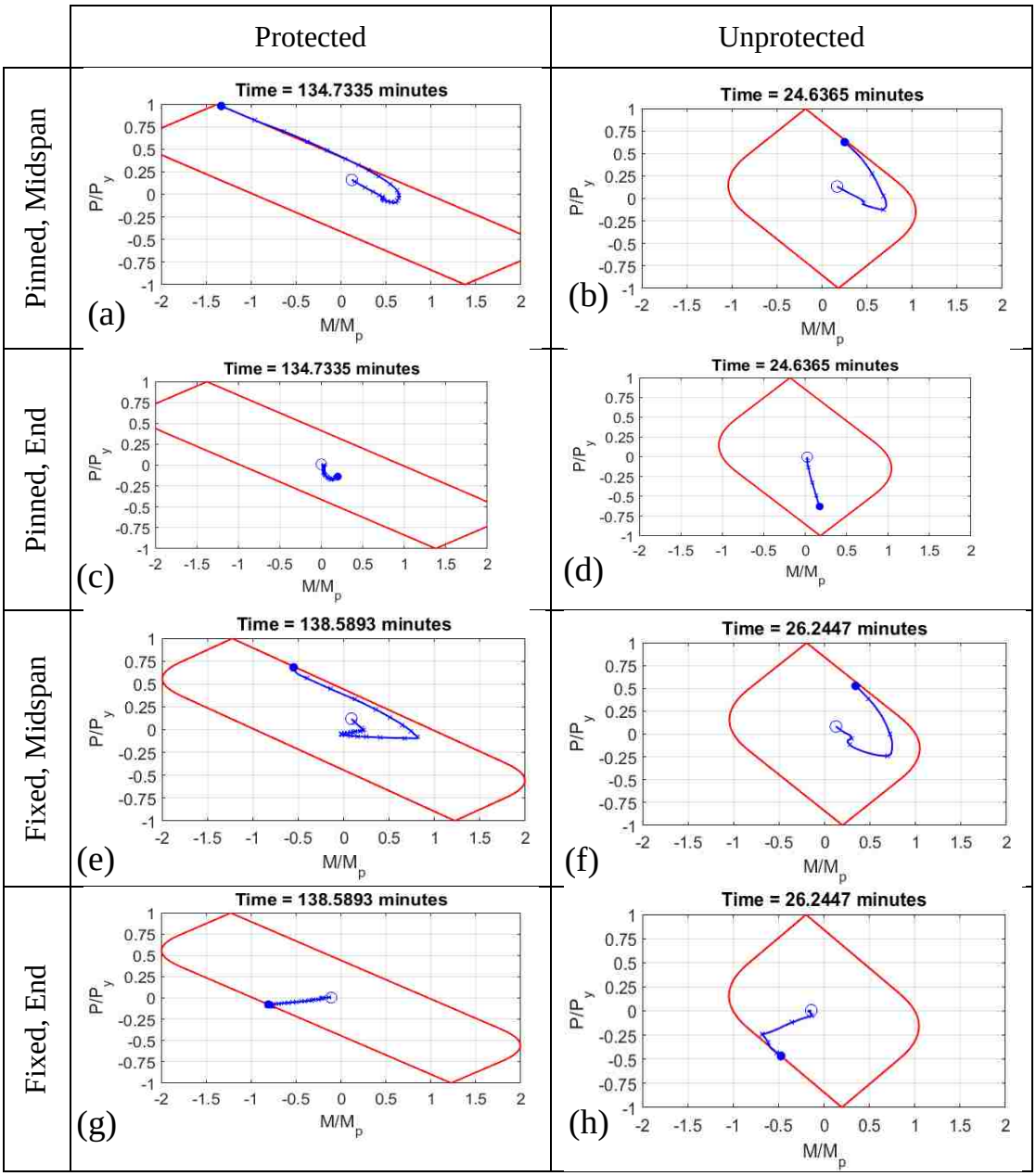

Fig. 3-20. Normalized P-M diagrams for the steel beam at runaway failure for the TT fiber-beam analyses.

Comparing **Fig. 3-20**(a) to (e) and **Fig. 3-20**(b) to (f), it is evident that the pinned beams are more flexible than the fixed beams. Both pinned models fail slightly before the fixed models, but the interaction curves develop in a similar manner and the load path follows a similar shape. The unprotected beam experiences a quicker change in axial and

moment usage shown by the spacing of the time markers being larger. For all the midspan models, a similar pattern is shown to occur at a different rate of time, with the duration extending in the presence of passive protection. The beam end models diagrams in **Fig. 3-20**(c), (d), (g), and (h) are again for the steel separated from the slab. At the connection, the slab takes effectively no force as the top of the cross section would be in tension and slab tensile strength is neglected. This is reasonable, as the slab in reality is unrestrained and unattached to the column. For the pinned cases (c) and (d), little moment develops and the modeling results are shown to not contact the failure envelope as connection compression increases with the increasing thermal load. The negative end moment in the fixed connection increases in magnitude as the bottom flange continues to be compressed by the increasing thermal load. Minimal net section axial force develops at the ends because the top flange tension must increase corresponding to the bottom flange compression to continue to carry the moment from the gravity loading. The unprotected beam end develops slightly more axial compression due to the rapid temperature increase of the bottom flange and web causing a larger jamming force of the cross section into the connection region.

3.5 Fire Resistance Rating Observations

Though these two models last for different durations, the test deflections are shown to be a function of beam temperature, also captured in the modeling techniques. **Fig. 3-21** shows the test data compared against the predictions generated using pure lumped mass temperatures of the bottom flange (a) and beam average (b) as the abscissa and two-dimensional model deflection as the ordinate. The test results show the thermal-structural relationship is captured very well in the models. Regardless of protection level or fire

duration, the beam deflection behavior corresponds almost directly to temperature. The lumped mass temperatures are conservative when compared to the actual test temperatures, so the failure time is, in turn, conservative. The ASTM E119 failure criteria are also shown on the plots to compare structural failure temperatures at the chosen applied load level with current thermal limit states provided. The thermal limit states classify a failure ~100°C (212°F) sooner than the structural models indicate.

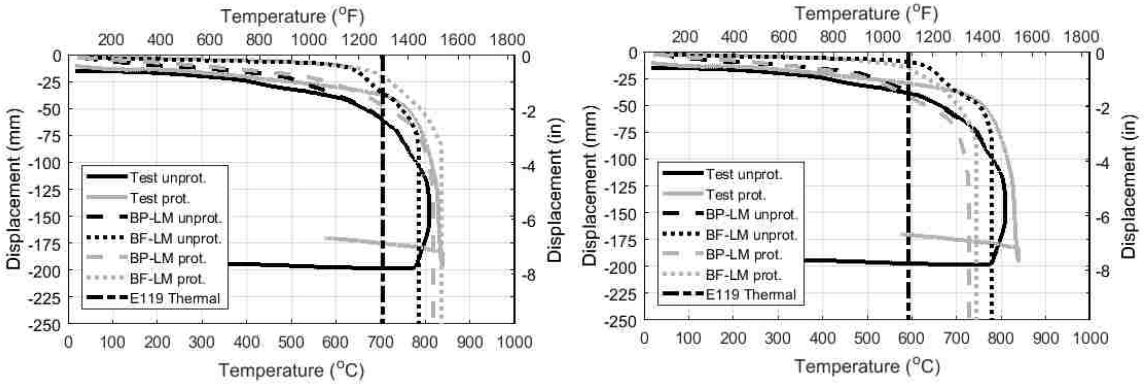

Fig. 3-21. Comparisons of deflections against (a) bottom flange and (b) beam average temperature

The ASTM E119 thermal failure criteria is compared to structural behavior in **Table 3-2**. The thermal lumped mass models for the protected beam indicate a thermal failure more than 40 minutes prior to the structural rating time, though the structure itself lasts much longer past the thermal criteria. This specimen was not rated per the design thermal criteria. A 2-hour thermal rating would have required thicker SFRM. This comparison is meant to highlight that a 2-hour structural rating is not equivalent to a 2-hour thermal rating. The assembly is roughly 1.5-hour rated thermally (estimated via a SAFIR 2D heat transfer analysis to determine when limiting temperatures would be reached for the given beam and protection level), which the test did meet, indicating the

SFRM was up to specification. This discrepancy between structural and thermal shows that simply performing a lumped mass thermal calculation for benchmarking against E119 data is insufficient in capturing structural performance. However, the thermal data could potentially be translated to structural data because the response is clearly a function of beam temperature. The unprotected specimen would not qualify for an hourly rating, so a structural analysis is inherently necessary in any performance-based design approach. The deflection limits from E119, maximum deflection of 87.0-mm (3.42-in) and maximum rate of deflection of 3.86 mm/min (0.15 in/min), are close to full structural runaway from a modeling perspective. In the experimental tests, runaway happens slightly later.

Table 3-2. Time needed to reach ASTM E119 thermal and deflection limits [2] (in minutes)

	By Temperature Limit		**By E119 Deflection Limit (Runaway)**						
			35% ϕM_n				**65% ϕM_n**		
Specimen	**Exp.**	**LM**	**Exp.**	**S-TT**	**B-TT (avg)**	**B-LM (avg)**	**S-TT**	**B-TT (avg)**	**B-LM (avg)**
Protected	88	75	130 (138)	134 (136)	132 (136)	114 (117)	86 (86)	98 (100)	84 (85)
Unprotected	12	12	22 (28)	25 (25)	25 (26)	25 (25)	14 (14)	15 (15)	15 (15)

Also shown in **Table 3-2** are the results from an additional batch of analyses run at 65% of the factored nominal moment capacity. These models represent a load level more consistent with in maximum in-service conditions. The deflection as a function of bottom flange temperature (a) and beam average temperature (b) are shown in **Fig. 3-22**. At the higher load level, the bottom flange models fail on average directly at the E119 maximum failure limit. For the beam average temperature, the E119 temperature limit is slightly conservative in all cases. These findings are promising in that they highlight the value of the thermal criteria as a potential indicator for structural behavior. The next steps lie in the

translation of E119 test data into actual performance. As discussed earlier, the thickness conversion equations for a presumably structurally-based rating did not lead to an equal rating using the thermal criteria.

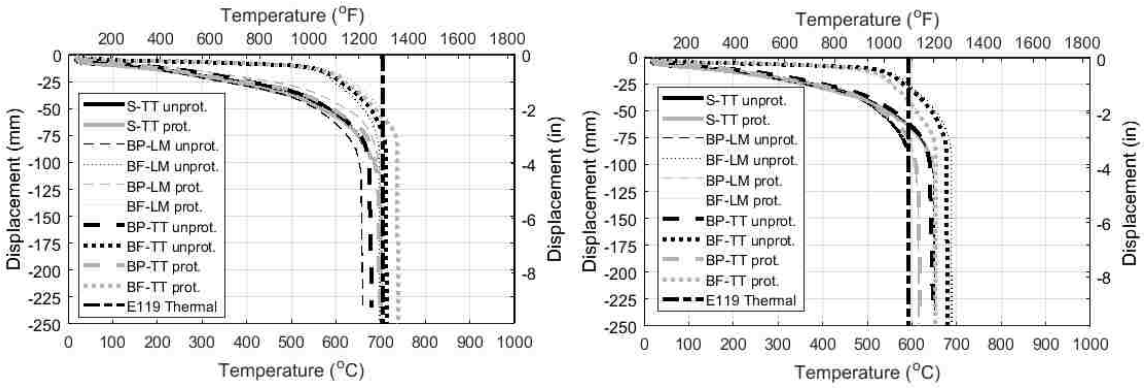

(a) (b)

Fig. 3-22. Comparisons of deflections against (a) bottom flange and (b) beam average temperature at 65% ϕM_n

Higher fidelity models exist to capture composite floor beam behavior, but there is little simplified, accepted criteria for practical implementation by the structural engineer in industry. There is a multitude of existing data for ASTM E119 tests, but these tests make many simplifications which draw away from the reality experienced in a built environment. However, the thermal criteria provided does lend some credence to structural behavior. Ideally, performance-based design techniques would leverage the vast quantity of standard fire test data available. The logical first step in developing simplified tools was to capture the associated structural mechanics in standard test a one-to-one comparison between protected and unprotected assemblies. The models developed have the potential to be used parametrically for longer spans, larger beam depths, varying end continuity conditions, and different fire scenarios (i.e. natural fires with a decay phase).

4.0 Realistic Fire Models

The previous section demonstrated the inconsistencies associated with the current standard fire rating process. The thermal models are reasonably accurate at conservatively predicting material temperatures. This, in turn, leads to structural models conservatively capturing deflection behavior and failure modes. The missing piece in design for fire is determining a realistic fire load. The standard curves currently in use fail to account for active protection intervention or specific compartment fuel and ventilation properties. This method is presumably conservative and the quantity of available data is vast, but the true structural behavior in the event of a fire is unknown. With the potential implementation of more accurate structural models, the fire model needs to be refined as well. The standard tests incorporate thermal limit states, which can potentially be leveraged into damage prediction and resilience calculations, as temperature has shown to be significant in determining the survival a structure. The goal of the realistic fire model analysis is to determine a correlation between the large amount of E119 data and actual structure performance.

Various levels of complexity exist when determining a realistic fire curve. A realistic fire was selected for heating an additional, leftover specimen at Lehigh based on preliminary parametric models that can be found in Kordosky [18]. The fire was essentially the E119 standard curve for 20 minutes followed by furnace shutoff (assuming active protection initiates). The parametric models have since been updated and are summarized here. Buchanan and Abu [59] was used as a reference for compartment calculations and decay rates excluding active fire protection. The experimental fire curve was also limited

by furnace capabilities, as there was no way to reliably control the decay phase once the fire was extinguished in the original furnace setup.

The furnace curve was based on a lightweight concrete compartment with the parameters for the respective fire curves given in **Table 4-1**. The fuel loads chosen are consistent with the study performed by Elhami Khorasani et al. [60] to indicate a typical range for office buildings. A corresponding fire model was constructed based on standard parameters of an office compartment fire via Eurocode 1 (EC1) methods [61]. OZone [40] was used to generate a comparable realistic fire curve, OZ1, that had a similar peak as the Eurocode model with active protection initiated. As the OZone model is more involved, parameters identical to the Eurocode model resulted in fire curves which peaked at a lower value. Ventilation was increased by increasing window dimension to bring the OZone fire peak closer to the Eurocode calculation. An additional OZone curve, OZ2, was created assuming the automatic water extinguishing system failed to activate, and the fire extinguishing was provided by a fire brigade which arrived later. The comparison of all fire curves is plotted in **Fig. 4-1**, showing that the furnace temperature resembles the E119 curve for the first 20 minutes, and lacks an extended decay phase. The Eurocode fire curve initially resembles the furnace, but cools more slowly. The OZone curves ramp up slower, and have a steeper decay phase more closely resembling the test curve than the Eurocode model.

Table 4-1. Compartment fire properties

	Fire Curve Models	
Compartment Materials	Eurocode	OZone
Density (kg/m^3)	1600	1600
Specific Heat (J/kg K)	840	840
Thermal Conductivity (W/mK)	0.8	0.8
Fuel Load (MJ/m^2)	500	800
Compartment Dimensions		
Room Length (m)	5	5
Room Width (m)	5	5
Room Height (m)	3	3
Total Window Width (m)	2.4	4
Window Height (m)	1.5	0.6

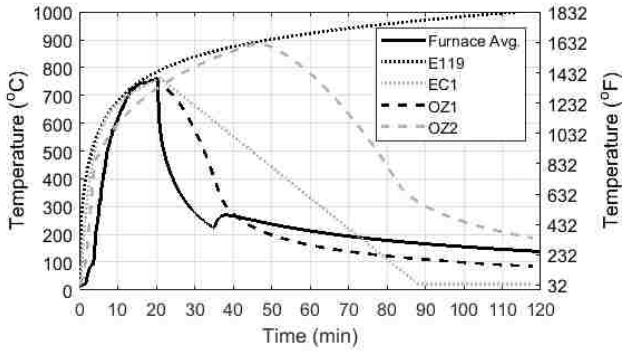

Fig. 4-1. Fire curve comparison

4.1 Comparison Test Summary

The realistic fire test specimen consisted of a 3.35-m (11-ft.-1-in.) long W8x10 beam with a 50.8-mm (2-in.) concrete slab on a 38.1-mm (1.5-in.) metal deck. The system was designed with 12.7-mm (½-in.) diameter, 50.8-mm (2-in.) long studs at 152.4-mm (6-in.) spacing to create composite action. The slab had W2.1 x W2.1, 6x6 welded wire reinforcement. W6x15 lateral bracing beams were attached to the specimen at third points to represent bracing from secondary floor beams and were terminated at the concrete deck

edge. The average concrete crushing strength at 40 days was determined to be 47.8 MPa (6.94 ksi) at 40 days via an average of three cylinders. The beam was connected to W10x26 columns at either end with a shear tab connection. Both the connection and column lengths within the furnace were again wrapped with ceramic blanket. The test setup was similar to that shown in **Fig. 3-1**. The shear strength of the bolts was determined with three tests and averaged to be 446.4 MPa (64.75 ksi) [62]. The specimen had been heated three times in the past and was left with a residual deflection of about 6.35 mm (1/2") at the beam center line as a result of its history, but was otherwise undamaged. The specimen was loaded with 20,017 N (4.5 kips) in two locations pushing the beam to 25% of the flexural capacity.

4.2 Thermal Modeling

4.2.1 Steel Thermal Profile

Once again, lumped mass calculations via the method described in Quiel and Garlock [44] were performed to estimate the steel temperature throughout the test. The steel beam is assumed to be heated on three sides. Convective heat transfer coefficients of 25 W/(m^2-K) and 9 W/(m^2-K) were used during the heating and cooling phase, respectively. In order to account for the slenderness of the section, a shadow effect factor was implemented to account for the ability of the bottom flange to shield the web from direct radiation from below. The shadow effect coefficient calculated in Eurocode 3 [13] is intended to be applied to a single average steel temperature, though the shadowing phenomenon chiefly affects the web temperature as the bottom flange shields the web from direct radiation based on heat coming from below. In order to account for this in the three-lumped mass approach being used, a shadow effect factor of 0.52 was applied to the web

temperature alone to give an overall steel temperature shadow effect of 0.78 which was calculated using Eurocode methods. The calculations can be seen in Appendix 3

4.2.2 Slab Thermal Profile

The physical slab used in thermal input files was modeled as a constant thickness made of 6 fibers based on the depth of the topping concrete above the deck ridges, rather than incorporating the slab ridges, for simplicity. To improve accuracy in the structural models, the slab referenced the temperatures from the 2D GiD corrugated heat transfer model rather than the 1D flat slab average discussed in 3.2.2. If resilience was a design goal, the flat slab average has been shown to be a reasonable approximation. In order to obtain the fiber temperatures, the slab was discretized as shown in **Fig. 4-2** and was fully exposed on its bottom surface to the test fire curve. The top of the slab was considered ambient (20°C) and was able to realistically release heat to the compartment above. The temperature in the corresponding structural thickness representation was calculated by averaging each layer in the regions above the ridge and above the trough (i.e. average of nodes 1 through 3 for the top fiber temperature) to determine a uniform, 6-fiber slab temperature profile. Sample slab temperatures found which correspond to the nodes in **Fig. 4-2** are shown in **Fig. 4-3**, alongside the measured top of slab temperature from the test.

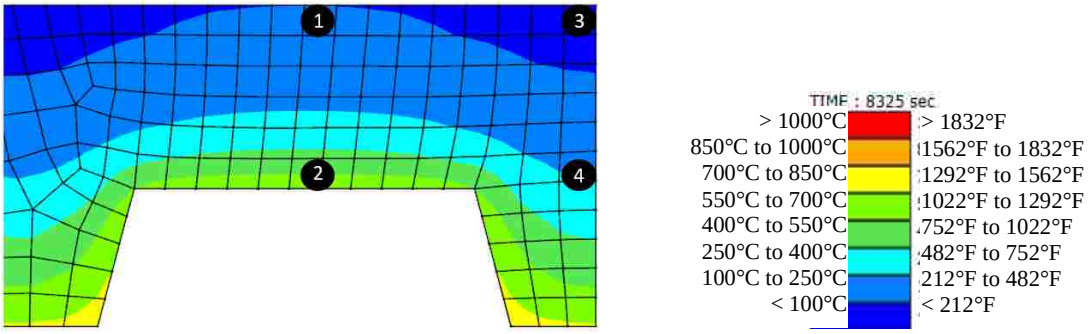

Fig. 4-2. Thermal slab model

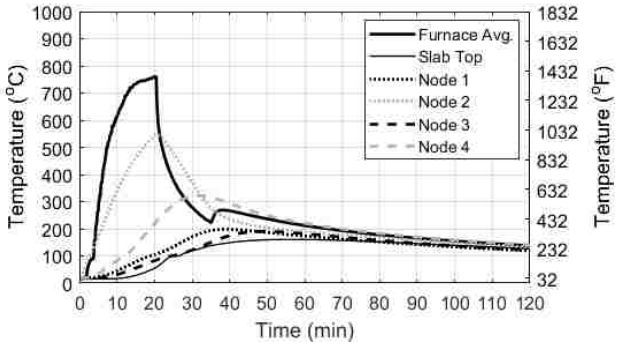

Fig. 4-3. Slab temperature from 2D thermal analysis

4.3 Structural Modeling

The structural modeling techniques first used identical thermal input (experimentally recorded temperatures) to determine temperature-dependent material properties through the length of the test. Lumped mass input was also calculated, similar to what was done for the standard fires. Again, both types of models discussed in 3.3 were created for the modeling of this test. Both models assumed fully-composite action, despite the ambient composite percentage being low. The assumption is conservative, as the steel heats up quicker than the slab, causing the composite utilization to trend full with an increase in temperature. It has been shown that ambient percent composite does not play a significant effect in ultimate failure time [22].

The percent composite of the beam over time was calculated using AISC Specification design equations [14]. **Fig. 4-4** shows the gain in composite action over time as steel temperature increased and relative strength decreased. At 20 minutes, the time of peak fire temperature, the beam is 75% composite. The shear stud temperature was calculated as an average of slab temperature and steel top flange temperature. In other studies [35], the stud temperature at a certain depth was shown to be fairly close to the slab temperature at the same depth, so this was a reasonable temperature assumption. The structural modeling results in upcoming sections further confirm the high level of composite action.

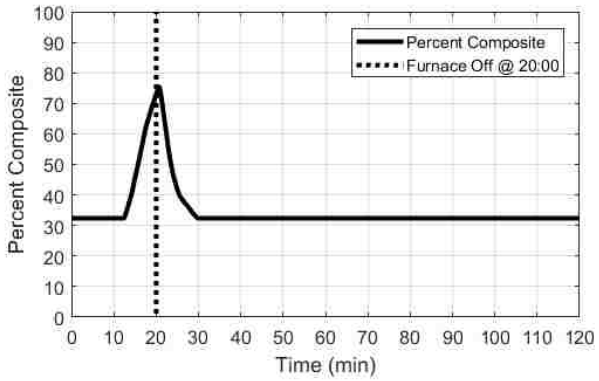

Fig. 4-4. Percent composite over time

4.3.1 Three-Dimensional Shell

The overall shell model discussion can be found in 3.3.2, with **Fig. 3-7** and **Fig. 3-9** highlighting the various parts, which are modified slightly for the W8x10 beam and thinner slab. The temperature linearly decreased over 7 transition sections from the location where the fiber blankets stopped about 355 mm (14”) from the beam end. The models showed similar results as the 14-transition models used previously, so for efficiency the thermal

gradient was made coarser. The slab shells were modeled separate from the steel and were connected via rigid connectors spaced at 0.154 m (6”) increments to simulate the shear studs. An artificially high modulus of elasticity of 500 GPa (72,519 ksi) was assigned to the studs to represent the confinement provided by the concrete. The studs were kept cold to be consistent with the rigidity assumed in the full-composite action with no slippage.

The shear tab connection was modeled using three truss elements (capable of axial force only) connected to the column. The stiffness of these elements was determined based on a simplified, component-based model [63]. The effective stiffness of the bolts in single shear was determined at the ambient condition for simplicity, as the connections remained below 300°C (572°F) for a majority of the test duration. The grade 8 bolts had material properties similar to A490 used in the reference examples. Stiffness calculations involved the bolt’s material properties, dimensions, and parameters calibrated from test results [55]. This calculation led to a stiffness value of 11.16 kN/mm per bolt. The truss element was assigned an elastic modulus of 500 GPa and the length of the element was defined as the distance from center of bolt hole to column centerline which was 166.4 mm (6.55”). The full calculations can be found in Appendix 4. The artificial cross-sectional area was sized to give a component with the stiffness equivalent to that of a shear tab bolt using the basic relationship for axial stiffness. The center element was slaved to the column in all degrees of freedom except in the axial direction, transferring the gravity load directly to eliminate the concern for shear transfer through truss elements. The upper and lower trusses were restrained from out of plane rotations. This simulated the flat section which would be restrained from buckling due to the presence of the tab plate. Translation was also permitted for the end nodes of the outer trusses so the connection could behave more realistically,

rotating about the center bolt with some stiffness provided by the upper and lower bolts extending and shortening. Shells coinciding with the location of the shear tab plate included additional tab thickness (12.6 mm) to add necessary stability to the connection zone to achieve numerical convergence at these locations of concentrated reaction force.

The average flange and web temperatures were applied over the majority of the beam length except for the 355-mm (14-in) segments on both ends that were covered in ceramic fiber blankets during the test. The average temperature measured at the connection during each test were input into the full section depth (web and both flanges) at the 50.8-mm (2-in) ends of the beam (i.e. the connection zone). The temperature in the web and flange plates over the remainder of the blanket-covered region was linearly increased from the connection temperature to their corresponding span temperature over the remainder of this transition, using seven transition regions as opposed to the fourteen used in earlier models. This is a coarser temperature transition, but validated model comparisons showed that fewer zones (over the same length) did not change the solution, so further analyses were carried out with only seven transitions regions. **Fig. 4-5** shows the detailed connection region in the shell models.

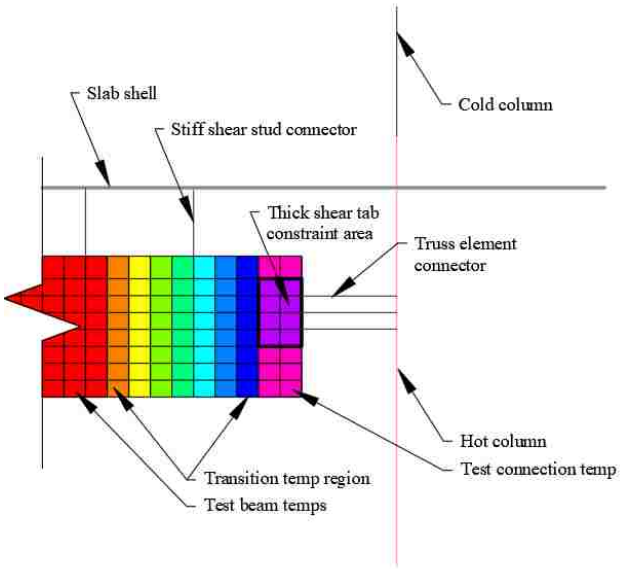

Fig. 4-5. SAFIR shell connection region

The inelastic analysis requires local imperfections to be implemented per Appendix 1 of AISC 2016 [14]. This aspect was especially important to consider due to the slender beam in this study. Similar to the 2D model, the top flange was not modified, as it is realistically unable to buckle. The amplitude of the imperfections in the web were calculated to be 0.3 mm (0.0118”), based on a value of d/500 (where d is the height of the web). The number of waves in the web were based on the web aspect ratio of a/b divided by 2, based on previous research [54]. For this beam, the aspect ratio is 1:20, therefore ten wavelengths were added into the web. Imperfections in the bottom flange were based on maintaining a right angle at the web-flange intersection. The flange tip imperfection amplitude was calculated as 0.2 mm (0.00787”). The steel beam was also given an initial out-of-straightness of 1/1000 of its length to allow for global buckling in the shell model.

Nodal relation constraints were necessary for the complex shell model to ensure the load transfer between the steel and slab through the rigid connector element was correctly

captured. Vertical displacement and rotation about the out of plane axis at nodes which were constrained in reality were defined as equal to a reference node. Namely, outer nodes in the top flange of the steel which coincided with the same longitudinal location as the shear stud point connection were slaved to the center where the connection occurred to represent the bracing provided by the deck rib on the flange. Similarly, the nodes in the slab which laid above the beam were slaved to the node within the slab where the stud attached. These modeling strategies created a more realistic representation of the support seen around the shear studs and helped to distribute the load over a larger area increasing numerical stability. Lastly, the W6 lateral bracing beams present were also modeled as constraints preventing out-of-plane bending at the points of contact.

4.3.2 Simplified, Two-Dimensional Fiber-Beam

The fiber-beam models were created using a perfectly pinned boundary condition between the beam and column to simulate the shear tab connection, based on the results from the standard fire models and tests. One additional fiber was included to model the equivalent WWR area to accurately capture the rebounding effects once the fire curve entered the decay phase. A total of 39 cross-sectional elements were used, 32 representing the steel beam, 6 the concrete, and 1 a smeared steel layer representing the equivalent area of WWR within the slab. The cross section is shown in **Fig. 4-6**. The entire composite system was modeled as one fiber-beam entity in the structural model. Formulating the cross-section in this manner inherently applied the assumption that the beam is fully composite throughout the test, since the complete fiber-beam section remained plane for the entire duration. Concrete tensile strength was neglected for simplicity. Models analyzed

at a tensile strength equal to 10% of the compressive strength were shown to not impact failure time. Columns were modeled with a heated portion having the measured test temperatures explicitly assigned, as this paper strives to capture beam mechanics with all else constant.

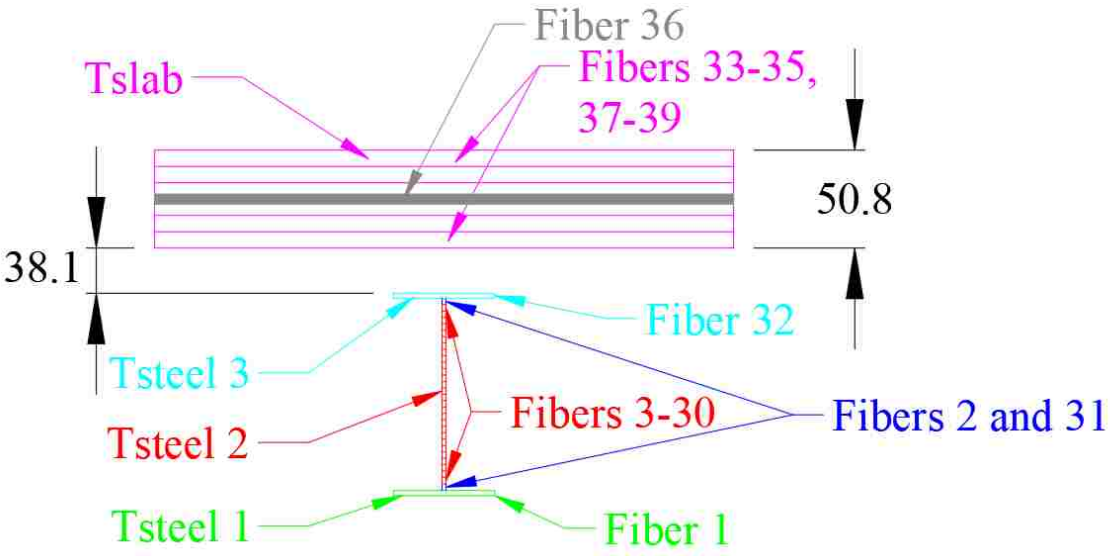

Fig. 4-6. Cross section of W8x10 fiber-beam model (dimensions in mm)

One of the modeling concerns for the W8x10 section was its slenderness. High levels of compression are seen in structural fire models as the beams tend to expand with simultaneously weakening structural properties due to a temperature increase, increasing the likelihood of local buckling. SAFIR provides a modified material type, STEELSL, to account for local instabilities based on an effective constitutive law which reduces the compressive strength, while leaving tensile behavior unaffected [51]. Two new materials were created, one for the web and one for the bottom flange, with the only additional parameters required being the respective b/t slenderness ratios. The top flange did not warrant the use of the specialized local buckling material, as it is assumed to be fully braced

by the deck. Local buckling checks were performed for models approaching runaway failure, but the STEELSL material was not explicitly assigned in the final stages to allow the solution to remain stable for the last few time steps while capturing the rapid deflection.

Similar to the thermal input described in 3.3, explicit measured test temperatures and lumped mass predictions were used for validation purposes. The bottom and top flange fibers were assigned the corresponding temperature-time histories. All web fibers were assigned the web temperatures, except for those directly adjacent to the flanges. These "transition" fibers were assigned an average of the web and respective flange temperature to smooth the thru-depth thermal gradient and improve numerical convergence. The breakdown of fiber temperatures is shown in **Fig. 4-6**.

4.4 Model Validation

Fig. 4-7 shows the predicted temperatures of the flanges and web based on the lumped mass calculation. The lumped mass predictions match the "ramp up" phase of the fire closely as well as the decay phase for the bottom flange. The lumped mass calculation results in web temperatures close to the data acquired. The bottom flange lumped mass is slightly cooler than the test results, but the top flange is hotter. Overall, the three lumped masses show good agreement with the test data.

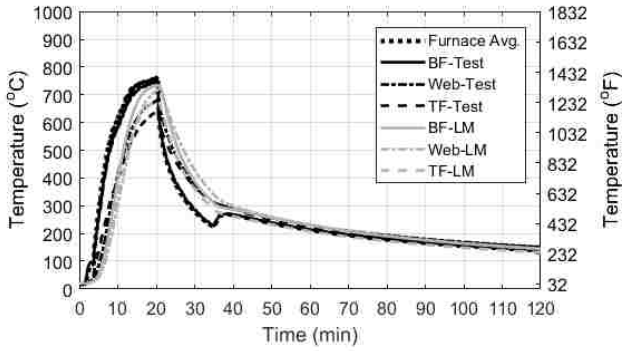

Fig. 4-7. Beam temperature comparison

The thermal models closely matched the test measurements, therefore structural responses were similar for models using explicit test temperatures and the three lumped mass calculation as thermal input. Assumptions discussed earlier simplified the structural model down to a practical level of complexity. All models with direct test temperature input behaved closer to the test data relative to their lumped-mass counterparts, as expected. **Fig. 4-8**(a) shows the comparison between the two structural models and the test. Both models lagged a bit behind the test deflection initially (due to the lumped mass calculation trailing the test fire). The lumped mass estimate still provides conservative peak deflection predictions for both the fiber-beam and the shell.

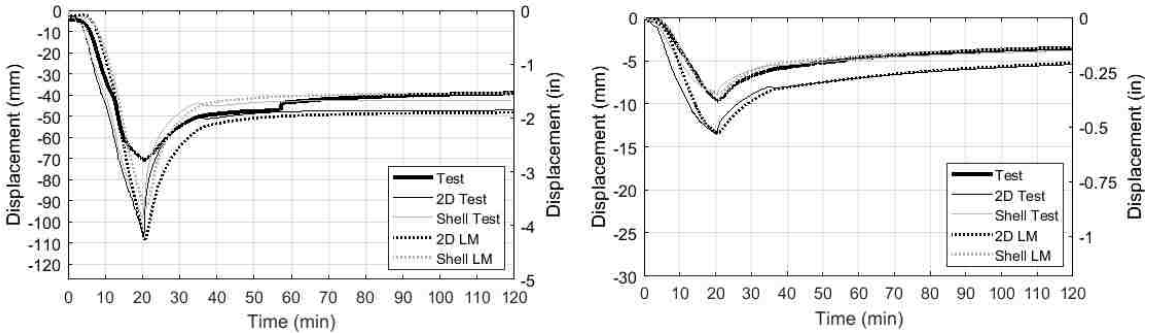

(a) (b)

Fig. 4-8. Deflection comparison for (a) midspan and (b) column lateral movement

The models are more flexible than what was actually seen in the test. The structural model assumes pinned boundary conditions, but the fixity of the connection may increase as the beam heats. Fixed boundary conditions were attempted but were shown to misrepresent the early behavior of the test. Additionally, the concrete was almost a decade older than when material tests were conducted and the possible strength gain is unaccounted for. Once the furnace is shutoff, the shell rebounds quicker to a residual plastic deflection matching the test data almost exactly, indicating the fully pinned assumption was sufficient. The two-dimensional model achieves a larger permanent deflection than the test, but is still a relatively close, conservative estimate. **Fig. 4-8**(b) shows the column horizontal displacement. Column displacement remained relatively small during this test. The negative displacement corresponds to the column bowing outward, due to beam expansion forces.

The shell model is more detailed than the 2D beam models, and but only offers a marginally better prediction of the composite floor system behavior from the test. The 2D beam models are able to provide extremely close and conservative estimates to the test data, and can be created far more efficiently. Both models verify that this assembly is able

to survive the assumed realistic fire curve, which accounts for compartmentation and ignition of active fire protection. This experiment had a slender beam and thin corrugated slab, but was still able to withstand a realistic fire without accounting for slab continuity or protection.

5.0 W8x10 Resiliency Study

Though the beam was able to survive, there is no consensus on the level of damage permissible after a fire. In the extreme event of a fire, there will most likely be some level of damage to the structure. In order for structural-fire engineering to be readily implemented, acceptable levels of performance must be quantified, similar to the progressive collapse/blast [17] or seismic [64] criteria. The resilience of systems could be calculated and different levels of protection could be selected based on a desired performance outcome, rather than an arbitrary "rating".

5.1 Analysis of Section Subject to Various Fire Curves

The experimental fire curve lacked an extended decay phase, as the burn dropped off rather abruptly due to furnace constraints. In order to further test the value in the structural model, the other preliminary fire curves discussed in *4.1* were applied computationally to the structure using the same three lumped mass approach. Calculated bottom flange temperatures associated with each fire curve are shown in **Fig. 5-1**. The relative relationship between flange temperatures were similar to the relationship between the fire curves themselves, as anticipated for unprotected steel.

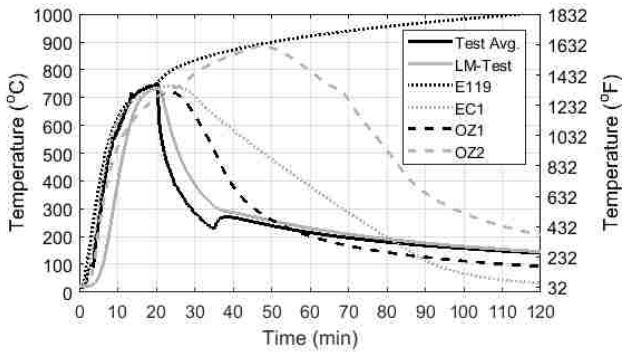

Fig. 5-1. Lumped mass bottom flange temperatures due to various fire curves

Connection zones in the shell model incorporated a reduced temperature to account for overshoot from primary member spray protection. Since the exact heat transfer was not modeled, observations from this test were used as the basis for the thermal model of the connections. The EC1 and OZone model with active protection (OZ1) peaked at a similar time and temperature, so it was deemed appropriate to use the exact temperature-time progression from the test. For the OZone model with no active protection (OZ2), the duration of the average temperature increase was extended to match the corresponding temperature peak, similar to the observed test data, at a rate of 12.1°C/min, shown in **Fig. 5-2**. The decay phase was assumed to intersect with the flattening portion of the fire to mimic the test observations for the furnace curve. ASTM E119 structural models reached runaway failure prior to OZ2 peak temperature. Therefore, the same connection temperatures were used as the model never reaches decay. There is no direct test comparison available for the plateauing slope in an E119 curve for wrapped connections as unprotected beams typically fail prior to reaching this point in the fire curve. For future modeling, more research should be conducted to verify the assumptions made for the connection region temperatures.

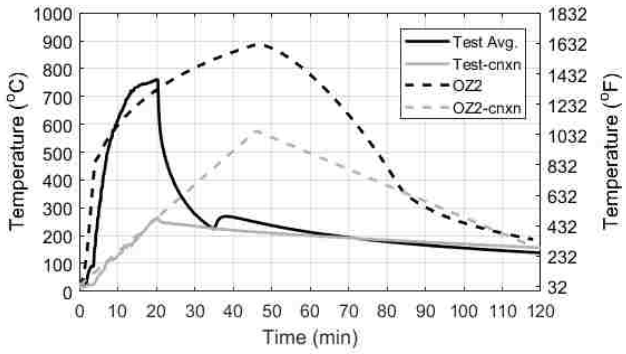

Fig. 5-2. Connection temperature generation

Fig. 5-3(a) shows the midspan displacements obtained from the pair of structural models discussed previously. The structural comparisons highlight the apparent sensitivity in choosing specific fire curves for unprotected models. OZ1 is the only model to survive the heating phase and rebound to a 50-cm residual deflection, similar to what was observed in the test. The EC1, OZ2, and E119 shell models reach runaway failure within nine minutes of each other, dependent on fire severity. The E119 and Eurocode curves have steeper ramp-up phases, so the beam properties more rapidly degrade, increasing the rate of deflection despite having a similar peak temperature. This indicates that time spent at high temperatures is also critical, not merely a flat peak temperature check as is currently performed in the E119 standard [2]. The 2D models follow the respective shells closely, showing the beginnings of runaway deflection, but lose stability before large deflections can be captured. These comparisons signify how close the chosen natural fire was to triggering a structural failure. However, this beam is smaller than most typical floor beams, so it serves as an upper bound of failure predictions for floor beams subject to this type of fire. Any larger beam would heat up more slowly under identical conditions. The findings indicate a more typical floor beam, even when left with minimal or no protection, could

potentially have significant fire resistance which could lead to resilience when natural fires are considered. There is currently no fire resistance attributed to unprotected members, though this slender unprotected member showed its survival potential.

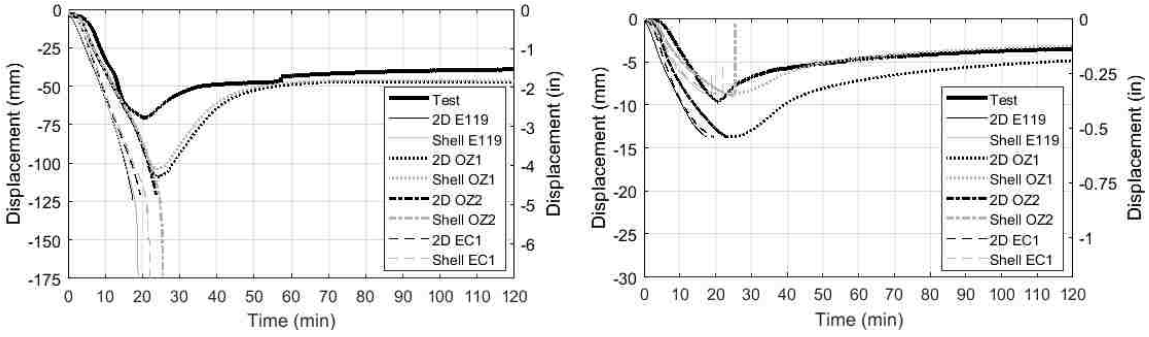

Fig. 5-3. Parametric deflection comparison for (a) midspan and (b) column lateral movement

Column deflection for the various tests was also compiled. The modeling results are shown in **Fig. 5-3**(b)**.** The W10x26 columns in each model deflected less than 15-cm (0.59-in) outward, and were a function of beam temperature causing thermal expansion forces. The shell models which reached runaway failure had a reversal in the direction of lateral column deflection as the beam plunged downward and pulled the columns inward.

The ASTM E119 standard fire test defines failure by thermal criteria as steel reaching an average temperature of 593.3°C (1100°F) or a maximum temperature of 704.4°C (1300°F), whichever occurs first. The standard E119 failure times associated with each fire model test are shown in **Table 5-1**. All models were governed by maximum average temperature criteria. These are compared with physical structural failure times. The corresponding maximum temperatures withstood in both structural models are also summarized.

Table 5-1. Comparison of structural failure time and ASTM E119 thermal failure criteria

Fire Curve	E119 thermal failure	Shell			2D Fiber-beam		
		Struct failure	Max. average temp. reached	Max. overall temp. reached	Struct failure	Max. avg temp. reached	Max. overall temp. reached
	min	**min**	**°C (°F)**	**°C (°F)**	**min**	**°C (°F)**	**°C (°F)**
Test	**13**	None	690 (1274)	752 (1386)	No structural failure, same thermal results as shell.		
LM-Test	**15**	None	708 (1306)	734 (1353)			
OZ1	**15**	None	698 (1288)	721 (1330)			
OZ2	**15**	25	716 (1321)	737 (1359)	23	708 (1306)	733 (1351)
Euro	**11**	22	721 (1330)	740 (1364)	19	701 (1294)	732 (1350)
E119	**11**	18	720 (1328)	742 (1368)	17	712 (1314)	736 (1357)

The W8x10 composite beam analyzed here failed by E119 standards somewhere between 11-15 minutes when subjected to any of the fire curves. However, three of these models were shown to structurally survive the respective natural fires applied with minimal residual deflection. The test reached average temperatures 100°C higher than specified allowable. On one hand, these results are excellent in showing the value of E119 thermal criteria in predicting a conservative failure capacity for fire loading. Conversely, the E119 standard does little to account for the resiliency and expected performance of a structural system. The vast amount of E119 thermal test data could potentially be leveraged for damage quantification calculations. These test models were for an unprotected, partially-restrained system. Typically, a minimum amount of protection will be applied to all floor beams, and actual beams are further restrained by slab continuity. Future work aims to develop models to account for the benefits of thermal restraint through anticipated tensile

membrane action. The survivability of an unprotected system opens the door for analyzing resiliency with varying levels of protection. A parametric study is conducted in the next section in order to quantify the potential decrease in structural damage as protection is increased.

5.2 Description of Protected Beam Models

ASCE 29-05 [5] states that in order to assign an hourly rating to a steel beam with SFRM protection based on the relative thickness conversion equations, the beam under consideration must be compact per AISC [14] requirements. Bearing this in mind, the W8x10 section would not technically qualify for an hourly rating via thickness conversions. However, in order to test relative levels of protection, thicknesses were calculated using UL Fire Resistance Directory Design D902 [42] tables and ASCE 29-05 conversion equations under full knowledge of the lack of UL certification. The 1-hr and 2-hr unrestrained/restrained thicknesses for a W8x28 provided in D902 were converted to equivalent thicknesses for the W8x10. The two levels of protections chosen were 13 mm (½") and 25 mm (1"). In order to determine actual hourly ratings for the systems, the E119 fire curve was applied via three-sided heating. The three lumped mass approach described earlier was used to determine steel temperatures over time associated with the computational E119 test, and ratings were dictated by when the limiting thermal criteria was reached. Based on this, the 13 mm thickness was rated at 45 minutes, while the 25 mm was rated at 1.5 hours. The goal of assigning ratings is to attempt to correlate what an E119 thermal rating means in terms of resilience.

5.3 Computational Results

Comparisons for the protected models included the same fire curves discussed throughout. For these cases, only the two-dimensional model was analyzed, as good agreement was shown with the shell in all unprotected cases, and the 2D model has a much lower computational cost. The setup of the structural model was identical to all unprotected cases, as the insulation offers no structural benefit. The bottom flange temperature results from the lumped mass thermal approach are shown in **Fig. 5-4**(a) and (b) for the 45- and 90-min rated assemblies, respectively. The highest temperatures result when the beam is heated with the E119 curve, as this curve has no decay phase and increases indefinitely. Overall, both levels of protection do a good job for the natural fires considering active protection (the test fire, Euro, and OZ1). Steel temperatures remain below 450°C (842°F) for the 45-min system and below 300°C (572°F) for the 90-min.

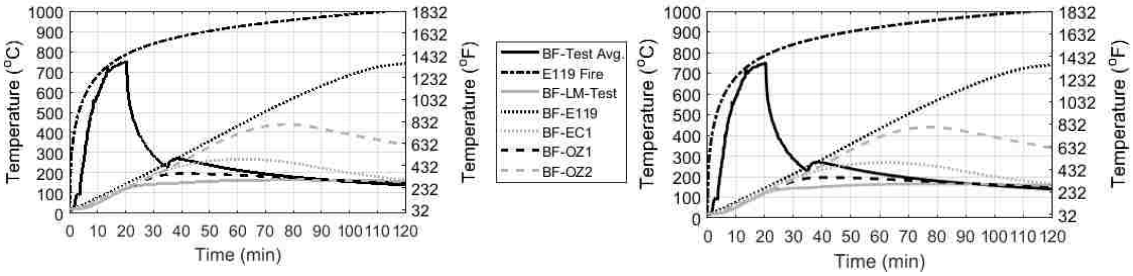

(a) (b)

Fig. 5-4. Bottom flange temperatures for ratings of (a) 45-min and (b) 90-min

An interesting effect of protection is the delay in peak steel temperature for the natural fires with decay phases. In most unprotected cases, the steel temperature peaks when the fire temperature peaks, with only a minor lag. The highest temperature peak of 684°C (1263°F) occurs for the 45-min rated OZ2 model near the 65 minute mark. The OZ2

fire curve peaks around 45 minutes, but the fire temperature remains warmer than the steel for an additional 20 minutes due to the addition of protection, causing extended heating. The 90-min OZ2 model reaches a peak temperature of 440°C (824°F) after 78 minutes, a full 30 minutes after the fire temperature begins to decay. The protected steel also experiences a much slower cooling phase when compared to the unprotected, holding the steel at high temperatures for longer. The low thermal conductivity of SFRM is beneficial for the heating process, but detrimental in the cooling phase as it prevents heat from easily escaping the steel.

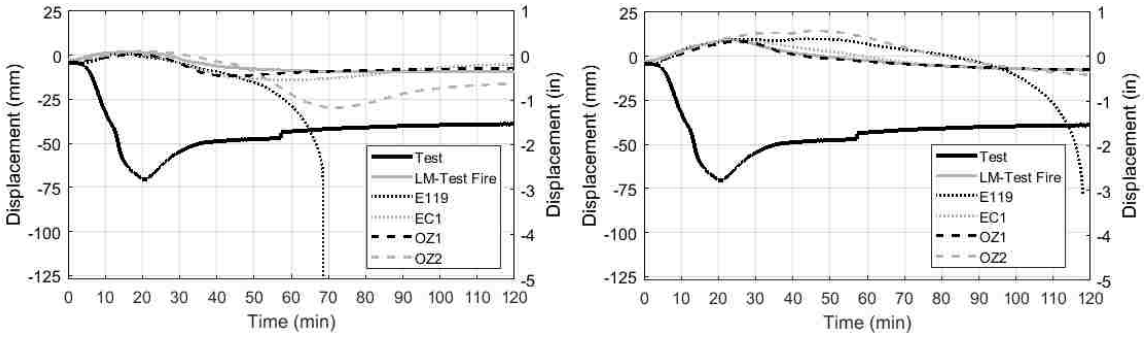

Fig. 5-5. Midspan deflections for ratings of (a) 45-min and (b) 90-min

Structural results for the 45-min protected models are shown in **Fig. 5-5**(a). Initially, the beam deflects upward from its loaded state as the section heats up more gradually. This can be attributed to the light section and idealized pin boundary conditions. The thermal gradient causes a moment reversal, and the elastic modulus begins to decrease at 100°C (212°F) allowing more flexibility in the system. Structural failure was reached for the E119 fire curve at 68 minutes, occurring via runaway deflection. The 45-min active protection models all have peak midspan deflections less than 14 mm (0.55”) occurring around maximum beam temperature, with residual deflections less than 9.0 mm (0.35”).

This is smaller than the permitted L/360 live load deflection of 9.2 mm (0.36”). The model without active protection, OZ2, reaches a peak deflection of 29.7 mm (1.17”) and then rebounds to 10.4 mm (0.41”) of residual deflection. OZ2 analyses were extended to 24 hours, shown in **Fig. 5-6**, to ensure the structure was stable and a final residual deflection was attained.

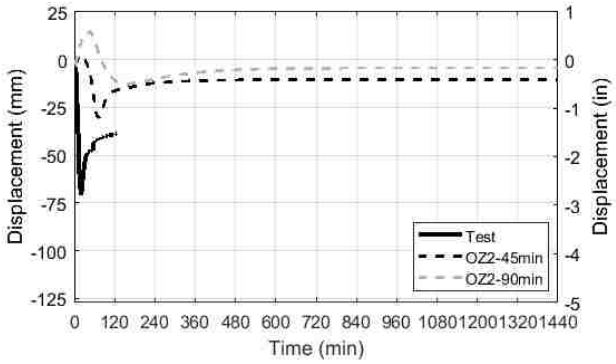

Fig. 5-6. OZ2 midspan deflections for protected beams

Fig. 5-5(b) shows the results for the 90-min rated floor beams. The thermal bowing is more pronounced for the higher protection, leading to a peak upward deflection of 14.7 mm (0.58”). The higher amount of protection on the beam leads to the slab heating up relatively faster than the steel when compared to other cases. For the thin slab system used in this test, the steel mesh is actually hotter than the bottom flange protected beam for about 45 minutes. The mesh tension reaches 85% of its Eurocode 3 temperature dependent proportional limit and does not experience permanent deformation. Structural failure by runaway deflection for the E119 curve occurred at 117 minutes. All other models, including OZ2, rebounded to a residual deflection of less than 7.9 mm (0.31”).

Once again, the E119 thermal failure criteria (see *5.4* for discussion) was compared to modeling results, shown in **Table 5-2**. Only one natural fire reached a limiting

temperature - the OZ2 beam with 45-min of SFRM protection at 57 minutes. The curves including the effects of active protection have peak temperatures almost 200°C below the E119 critical average of 593°C. A minimal amount of passive protection being applied allows the structure to survive the fire. An hourly rating of 90-min keeps the three models with active protection below 260°C, which, by Eurocode standards, leads to a temporary yield strength (proportional limit) near 70% of ambient. Ultimate strength remains unaffected at temperatures below 400°C. The modulus of elasticity drops to around 85% of ambient for a few minutes. The structure performs well in all natural fires, with most of them remaining below service level deflection. This is granting the conservancy provided by leaving the slab edge unrestrained, and highlights the need for more research in capturing behavior under natural fires.

Table 5-2. Protected results summary for 45-min of protection

	45-min SFRM protection			**90-min SFRM protection**		
Fire Curve	**E119 thermal failure**	**Struct. failure**	**Max. avg (overall) temp. reached**	**E119 thermal failure**	**Struct. failure**	**Max. avg (overall) temp. reached**
	min	**Min**	**°C (°C)**	**min**	**min**	**°C (°C)**
E119	**51**	68	692 (747)	**93**	117	686 (737)
OZ2	**57**	None	627 (685)	**None**	None	411 (440)
EC1	**None**	None	231 (253)	**None**	None	161 (165)
OZ1	**None**	None	315 (350)	**None**	None	185 (196)
LM-Test	**None**	None	404 (438)	**None**	None	255 (268)

Quantifying structural resilience implies correlating certain levels of damage with anticipated structural behavior. For these preliminary comparisons, damage is described as simply level I, II, or III. Level III indicates collapse. Level I indicates little to no residual deflection, defined as being less than the typical allowable service level deflections (L/360)

seen in design. Level II represents significant damage as anything greater than allowable service deflection but less than ultimate collapse. The steel beam most likely experienced some plasticity in this case creating permanent residual deflections and would most likely require rehabilitation. As more research is performed, these levels will be refined as the suitability of these analysis methods when applied to longer lengths, deeper beams, and realistic slab continuity conditions is confirmed.

Table 5-3 summarizes the levels of damage seen for the unprotected, 45-min, and 90-min 2D structural models, as well as the maximum average steel temperatures reached during analysis. A minimal amount of protection (45-min) allows for survival with little to no damage in all cases where active protection initiates, and causes the beam to withstand the OZ2 curve associated with sprinkler failure. A more substantial amount of protection (90-min) ensures survival with little to no damage in any of the realistic fire curves analyzed. One important observation is that the E119 structural failure temperatures for the protected models are lower than temperatures seen in unprotected models which survived. This can be attributed to the duration of heating. This finding reinforces the belief that time spent at heightened temperatures also plays a role in beam strength and resilience, rather than a basic peak temperature check as is prescribed in E119. The relationship between the temperature-time history and survivability will be analyzed in future work, with the hopes of leveraging E119 test results of various levels of protection as a gauge for true structural performance.

Table 5-3. Damage level comparison

Fire Curve	Unprotected	45-min	90-min
	Damage Level (maximum average steel temp. °C)	**Damage Level** (maximum average steel temp. °C)	**Damage Level** (maximum average steel temp. °C)
E119	**III** (703)	**III** (692)	**III** (686)
OZ2	**III** (701)	**II** (627)	**I** (411)
Euro	**III** (699)	**I** (231)	**I** (161)
OZ1	**II** (698)	**I** (315)	**I** (185)
LM-Test	**II** (708)	**I** (404)	**I** (255)

This approach demonstrates the potential for a stochastic risk analysis for exposure to realistic fire curves. Levels of protection could be tailored to different spans and sections. This may not cause any changes in the current levels of protection applied; however, improved understanding of the structural response with varying levels of protection in multiple fire scenarios would provide a basis for more accurate insurance estimates. Additionally, there may be justification for increasing protection in some cases to increase resilience (i.e. specifying an amount that, even in the event of active protection failure, will prevent any natural fires from reaching critical temperatures responsible for permanent plastic deformations). Upcoming work will establish performance-based design damage categories for use by the practicing structural engineer.

6.0 Conclusions and Future Work

This computational resiliency study analyzed three separate, partially composite, partially restrained large-scale composite floor beams subjected to the E119 fire curve and a realistic fire utilizing varying complexity thermal and structural models. The temperatures of the beam were compared with MATLAB lumped mass calculations. The top of slab temperature was compared with numerical heat transfer models in SAFIR. The

modeling efforts correlated reasonably well with the test data and were conservative. Various alternative natural fire curve formulations were analyzed as well. A parametric study was conducted under two additional levels of protection in order to quantify the potential resilience of the base structural system. Damage levels were created to compare performance between varying protections. The modeling and test observations indicate:

1. A three-dimensional shell model captured the test behavior with identical thermal input (using measured test temperatures).
2. Two-dimensional fiber-beam structural models were shown to conservatively predict structural failure times with a simple, blind one-dimensional lumped mass calculation, and the only knowledge of the test being the anticipated fire curve and ambient conditions.
3. The lumped mass calculations provide flexibility to create efficient predictions of steel temperatures with varying exposure, allowing for scaling based on top flange coverage, beam shadow effect, etc.
4. Calculating the temperature of the bare steel beam is simpler than the protected beam, and more research needs to be conducted in order to obtain better temperature predictions for SFRM protected beams (though the current predictions are conservative).
5. Temperature comparisons between the 1D slab thermal model and the test top of slab showed the slab surface trended towards the temperature seen in the thicker models.
6. The simplified lumped mass models are able to predict a plastically dominant runaway failure within 30 minutes for the selected protected beam and 5 minutes for the unprotected beam.

7. ASTM E119 thermal criteria was shown to be conservative in failure prediction for all cases, but fails to explicitly inform the user about potential survivability once fire decay is introduced. Time spent at higher temperatures (500-600°C) contributes to strength and in turn, resilience, which is unaccounted for in the maximum allowable temperature criteria prescribed in E119
8. When minimal SFRM protection is applied (45-min hourly rating), all W8x10 structural models subjected to realistic fire scenarios survive. Models considering active protection initiation resulted in little to no residual beam deflection, while the model considering sprinkler failure has a nominal residual deflection.
9. When significant SFRM protection is applied (90-min hourly rating), all W8x10 structural models of realistic fire scenarios result in little to no residual deflections.
10. Increasing protection lowers peak steel temperature in structural fire models, but extends the duration to peak temperature as the fire remains hotter than the steel for longer.
11. As protection increases in E119 test simulations, peak temperature at structural failure decreases. The unprotected W8x10 specimen fails a computational E119 fire at a maximum average steel temperature of 712°C, the 45-min at 675°C, and the 90-min at 659°C.

The models serve as benchmarks for expanding E119 test data into performance-based design formulations. Future modeling work and experiments will incorporate longer spans, local stability and other modes of damage, as well as more realistic slab restraint conditions in the models and tests to broaden the lumped mass calculation applications. Additional modeling will be conducted to focus on specific connection requirements for

beams subject to fire. Larger simulations of multi-story buildings will be run to better capture axial and rotational stiffness at beam ends during the fire, and possibly account for the benefits to the structural system by tensile membrane action.

7.0 References

[1] International Code Council (ICC), International Building Code, 2014.

[2] ASTM Standard E119-18, Standard Test Methods for Fire Tests of Building Construction and Materials, ASTM International, West Conshohocken, PA, 2018. doi:10.1520/E0119-18CE01.

[3] International Organization for Standardization, ISO 834-13:2019, 2019. http://www.iso.org/cms/render/live/en/sites/isoorg/contents/data/standard/06/64/66439.html (accessed June 18, 2019).

[4] Underwriters Laboratories Inc., UL Product Spec, (n.d.). http://productspec.ul.com/index.php (accessed June 18, 2019).

[5] American Society of Civil Engineers, Society of Fire Protection Engineers, Structural Engineering Institute, eds., Standard calculation methods for structural fire protection (ASCE/SEI/SFPE 29-05), American Society of Civil Engineers, Reston, Va, 2007.

[6] J. Ruddy, J. Marlo, S. Ioannides, F. Alfawakhiri, Steel Design Guide 19: Fire Resistance of Structural Steel Framing, (2003).

[7] R.G. Gewain, E.W. Troup, Restrained fire resistance ratings in structural steel buildings, ENGINEERING JOURNAL-AMERICAN INSTITUTE OF STEEL CONSTRUCTION. 38 (2001) 78–89.

[8] C.G. Bailey, T. Lennon, D.B. Moore, The behaviour of full-scale steel-framed buildings subjected to compartment fires, The Structural Engineer. 77 (1999) 15–21.

[9] F. Wald, L. Simões da Silva, D.B. Moore, T. Lennon, M. Chladná, A. Santiago, M. Beneš, L. Borges, Experimental behaviour of a steel structure under natural fire, Fire Safety Journal. 41 (2006) 509–522. doi:10.1016/j.firesaf.2006.05.006.

[10] R. Bletzacker, Fire resistance of protected steel beam floor and roof assemblies as affected by structural restraint, in: Symposium on Fire Test Methods—Restraint & Smoke 1966, ASTM International, 1967.

[11] C.J. Carter, F. Alfawakhiri, Restrained or Unrestrained?, Modern Steel Construction. (2013).

[12] P.J. Moss, A.H. Buchanan, J. Seputro, C. Wastney, R. Welsh, Effect of support conditions on the fire behaviour of steel and composite beams, Fire and Materials. 28 (2004) 159–175. doi:10.1002/fam.855.

[13] European Committee for Standardization (CEN), Eurocode 3: Design of steel structures - Part 1-2: General rules - Structural fire design, Brussels, Belgium, 2005.

[14] American Institute of Steel Construction, Specification for Structural Steel Buildings, ANSI/AISC 360-16, 2016.

[15] American Society of Civil Engineers, Minimum design loads for buildings and other structures, American Society of Civil Engineers : Structural Engineering Institute, 2016.

[16] K.J. LaMalva, ed., Manual of Practice 138: Structural Fire Engineering, American Society of Civil Engineers, Reston, Virginia, 2018.

[17] GSA, Alternate path analysis & design guidelines for progressive collapse resistance, Washington, D.C, 2011.

[18] A. Kordosky, Experimental and Computational Investigation of Composite Beam Response to Fire, Lehigh University, 2017.
[19] V.K.R. Kodur, M. Naser, P. Pakala, A. Varma, Modeling the response of composite beam–slab assemblies exposed to fire, Journal of Constructional Steel Research. 80 (2013) 163–173. doi:10.1016/j.jcsr.2012.09.005.
[20] E.C. Fischer, A.H. Varma, Fire behavior of composite beams with simple connections: Benchmarking of numerical models, Journal of Constructional Steel Research. 111 (2015) 112–125. doi:10.1016/j.jcsr.2015.03.013.
[21] K.L. Selden, A.H. Varma, Flexural Capacity of Composite Beams Subjected to Fire: Fiber-Based Models and Benchmarking, Fire Technology. 52 (2016) 995–1014. doi:10.1007/s10694-016-0565-7.
[22] W. Wang, K. Wang, M.D. Engelhardt, G. Li, Behavior of Steel–Concrete Partially Composite Beams Subjected to Fire—Part 2: Analytical Study, Fire Technology. 53 (2017) 1147–1170. doi:10.1007/s10694-016-0624-0.
[23] R. Zaharia, C. Vulcu, O. Vassart, T. Gernay, J.M. Franssen, Numerical analysis of partially fire protected composite slabs, Steel and Composite Structures. 14 (2013) 21. doi:10.12989/scs.2013.14.1.021.
[24] J. Jiang, A. Usmani, G.-Q. Li, Modelling of Steel-Concrete Composite Structures in Fire Using OpenSees, Advances in Structural Engineering. 17 (2014) 249–264. doi:10.1260/1369-4332.17.2.249.
[25] Elhami Khorasani Negar, Gernay Thomas, Fang Chenyang, Parametric Study for Performance-Based Fire Design of US Prototype Composite Floor Systems, Journal of Structural Engineering. 145 (2019) 04019030. doi:10.1061/(ASCE)ST.1943-541X.0002315.
[26] S. Lamont, B. Lane, G. Flint, A. Usmani, Behavior of Structures in Fire and Real Design - A Case Study, Journal of Fire Protection Engineering. 16 (2006) 5–35. doi:10.1177/1042391506054038.
[27] Z. Huang, I.W. Burgess, R.J. Plank, Modeling Membrane Action of Concrete Slabs in Composite Buildings in Fire. II: Validations, Journal of Structural Engineering. 129 (2003) 1103–1112. doi:10.1061/(ASCE)0733-9445(2003)129:8(1103).
[28] S. Lamont, M. Gillie, A.S. Usmani, Composite steel-framed structures in fire with protected and unprotected edge beams, Journal of Constructional Steel Research. 63 (2007) 1138–1150. doi:10.1016/j.jcsr.2006.10.001.
[29] C.G. Bailey, Membrane action of slab/beam composite floor systems in fire, Engineering Structures. 26 (2004) 1691–1703. doi:10.1016/j.engstruct.2004.06.006.
[30] J.C. Silva, A. Landesmann, Performance-based analysis of steel–concrete composite floor exposed to fire, Journal of Constructional Steel Research. 83 (2013) 117–126. doi:10.1016/j.jcsr.2013.01.009.
[31] E.I. Wellman, A.H. Varma, R. Fike, V. Kodur, Experimental Evaluation of Thin Composite Floor Assemblies under Fire Loading, Journal of Structural Engineering. 137 (2011) 1002–1016. doi:10.1061/(ASCE)ST.1943-541X.0000451.
[32] Z. Huang, I. Burgess, R. Plank, C. Bailey, Comparison of BRE simple design method for composite floor slabs in fire with non-linear FE modelling, Fire and Materials. 28 (2004) 127–138. doi:10.1002/fam.847.

[33] S. Quiel, M. Garlock, Parameters for Modeling a High-Rise Steel Building Frame Subject to Fire, Journal of Structural Fire Engineering. 1 (2010) 115–134. doi:10.1260/2040-2317.1.2.115.
[34] W. Wang, M.D. Engelhardt, G. Li, G. Huang, Behavior of Steel–Concrete Partially Composite Beams Subjected to Fire—Part 1: Experimental Study, Fire Technology. 53 (2017) 1039–1058. doi:10.1007/s10694-016-0618-y.
[35] K.L. Selden, E.C. Fischer, A.H. Varma, Experimental Investigation of Composite Beams with Shear Connections Subjected to Fire Loading, Journal of Structural Engineering. 142 (2016) 04015118. doi:10.1061/(ASCE)ST.1943-541X.0001381.
[36] E. Ellobody, Nonlinear behaviour of unprotected composite slim floor steel beams exposed to different fire conditions, Thin-Walled Structures. 49 (2011) 762–771. doi:10.1016/j.tws.2011.02.002.
[37] J.-M. Franssen, T. Gernay, Modeling structures in fire with SAFIR®: theoretical background and capabilities, Journal of Structural Fire Engineering. 8 (2017) 300–323. doi:10.1108/JSFE-07-2016-0010.
[38] O. Mirza, B. Uy, Behaviour of headed stud shear connectors for composite steel–concrete beams at elevated temperatures, Journal of Constructional Steel Research. 65 (2009) 662–674. doi:10.1016/j.jcsr.2008.03.008.
[39] L. Choe, S. Ramesh, M. Seif, M.S. Hoehler, W. Grosshandler, J. Gross, M. Bundy, Fire Performance of Long-Span Composite Beams with Gravity Connections, in: 10th International Conference on Structures in Fire (SiF18), Belfast, UK, 2018: p. 8.
[40] J.-F. Cadorin, D. Pintea, J.-C. Dotreppe, J.-M. Franssen, A tool to design steel elements submitted to compartment fires—OZone V2. Part 2: Methodology and application, Fire Safety Journal. 38 (2003) 429–451. doi:https://doi.org/10.1016/S0379-7112(03)00015-8.
[41] M.R. Vinnakota, C.M. Foley, S. Vinnakota, Design of Partially or Fully Composite Beams with Ribbed Metal Deck Using LRFD Specifications, ENGINEERING JOURNAL. (1988) 19.
[42] Underwriters Laboratories Inc., Fire Resistance Directory Volume 1: Design D902, (2016).
[43] Isolatek International, CAFCO 300 Spray-Applied Fireproofing, (2016).
[44] S.E. Quiel, M.E.M. Garlock, Closed-Form Prediction of the Thermal and Structural Response of a Perimeter Column in a Fire, The Open Construction and Building Technology Journal. 4 (2010) 15.
[45] The MathWorks, Inc., MATLAB and Statistics Toolbox, Natick, Massachussetts, 2017.
[46] V.K.R. Kodur, A.M. Shakya, Effect of temperature on thermal properties of spray applied fire resistive materials, Fire Safety Journal. 61 (2013) 314–323. doi:10.1016/j.firesaf.2013.09.011.
[47] J.I. Ghojel, M.B. Wong, Three-sided heating of I-beams in composite construction exposed to fire, Journal of Constructional Steel Research. 61 (2005) 834–844. doi:10.1016/j.jcsr.2004.11.006.
[48] International Center for Numerical Methods in Engineering (CIMNE, GiD: The personal pre and postprocessor, Barcelona, Spain, 2016. www.gidhome.com.

[49] European Commission for Standardization, EN 1992-1-2: Eurocode 2: Design of concrete structures - Part 1-2: General rules - Structural fire design, European Commission for Standardization, 2008.
[50] Y. Lee, M.-S. Choi, S.-T. Yi, J.-K. Kim, Experimental study on the convective heat transfer coefficient of early-age concrete, Cement & Concrete Composites. 31 (2009) 60–71. doi:https://doi.org/10.1016/j.cemconcomp.2008.09.009.
[51] J.-M. Franssen, B. Cowez, T. Gernay, Effective stress method to be used in beam finite elements to take local instabilities into account, Fire Safety Science. 11 (2014) 544–557. doi:DOI: 10.3801/IAFSS.FSS.11-544.
[52] P.V. Real, P.A.G. Piloto, J.-M. Franssen, A new proposal of a simple model for the lateral-torsional buckling of unrestrained steel I-beams in case of fire: experimental and numerical validation, Journal of Constructional Steel Research. 59 (2003) 179–199.
[53] K.L. Selden, STRUCTURAL BEHAVIOR AND DESIGN OF COMPOSITE BEAMS SUBJECTED TO FIRE, Ph. D. Thesis, Purdue University, 2014. https://docs.lib.purdue.edu/dissertations/AAI3669546/.
[54] S.E. Quiel, M.E.M. Garlock, Calculating the buckling strength of steel plates exposed to fire, Thin-Walled Structures. 48 (2010) 684–695. doi:10.1016/j.tws.2010.04.001.
[55] R.M. Peixoto, M.S. Seif, L.C.M. Vieira Jr., Double-shear tests of high-strength structural bolts at elevated temperatures, Fire Safety Journal. 94 (2017) 8–21. doi:10.1016/j.firesaf.2017.09.003.
[56] L. Yu, K.H. Frank, Shear Behavior of A325 and A490 High-Strength Bolts in Fire and Post-Fire, ENGINEERING JOURNAL. 46 (2009) 99–106.
[57] F.M. Block, J.B. Davison, I.W. Burgess, R.J. Plank, Principles of a component-based connection element for the analysis of steel frames in fire, Engineering Structures. 49 (2013) 1059–1067. doi:10.1016/j.engstruct.2012.07.025.
[58] M.E. Garlock, S.E. Quiel, Plastic Axial Load and Moment Interaction Curves for Fire-Exposed Steel Sections with Thermal Gradients, Journal of Structural Engineering. 134 (2008) 874–880. doi:10.1061/(ASCE)0733-9445(2008)134:6(874).
[59] A.H. Buchanan, A. Abu, Structural design for fire safety, Second edition, John Wiley & Sons Inc, Chichester, West Sussex, United Kingdom, 2017.
[60] N. Elhami Khorasani, M. Garlock, P. Gardoni, Fire load: Survey data, recent standards, and probabilistic models for office buildings, Engineering Structures. 58 (2014) 152–165. doi:10.1016/j.engstruct.2013.07.042.
[61] European Committee for Standardization (CEN), Eurocode 1: Actions on structures - Part 1-2: General actions - Actions on structures exposed to fire, Brussels, Belgium, 2002. http://www.phd.eng.br/wp-content/uploads/2015/12/en.1991.1.2.2002.pdf (accessed November 28, 2017).
[62] N.D. Catella, The Development of a Modular Furnace for Structural Fire Testing and a Study of Steel Shear Tab Connections' Behavior in Fire, Lehigh University, 2008.
[63] J.M. Weigand, R. Peixoto, L.C.M. Vieira Jr., J.A. Main, M. Seif, An empirical component-based model for high-strength bolts at elevated temperatures, Journal of

Constructional Steel Research. 147 (2018) 87–102. doi:https://doi.org/10.1016/j.jcsr.2018.03.034.
[64] American Society of Civil Engineers, ed., Seismic rehabilitation of existing buildings (ASCE/SEI 41), American Society of Civil Engineers, Reston, Va, 2007.

Vita

Michael Miroslav Drury, the son of Renata Drury and the late Michael Edward Drury, was born in Easton, PA on December 29th, 1994. He was raised in Saylorsburg, PA where he graduated from Pleasant Valley High School in 2013. Michael received his Bachelors of Science in Civil Engineering from Lehigh University in 2017. He has completed internships with Langan Engineering and Environmental Services and Simpson, Gumpertz, and Heger. Michael will receive his Master of Science in Structural Engineering in 2019 and will remain at Lehigh upon graduation to complete a PhD in Structural Engineering.

Appendix 1: W12x26 Ambient Calculations

Calculate moment capacity of W12x26 composite beam $L := 11\ ft$

$fy := 50000\ \frac{lb}{in^2}$ $f_u := 65000\ \frac{lb}{in^2}$ $E_s := 29 \cdot 10^6\ \frac{lb}{in^2}$

$As := 7.65\ in^2$ $d := 12.2\ in$ $I_x := 204\ in^4$ $b_{fl} := 6.49\ in$ $t_{fl} := 0.38\ in$ $t_{web} := 0.23\ in$

$T := fy \cdot As = (3.825 \cdot 10^5)\ lb$

$f'c := 4000\ \frac{lb}{in^2}$ $w_c := 120\ \frac{lb}{ft^3}$ $E_c := 33 \cdot 120^{1.5} \cdot \sqrt{4000}\ \frac{lb}{in^2} = (2.744 \cdot 10^6)\ \frac{lb}{in^2}$

$b := min\left(2 \cdot \frac{L}{8}, 10\ ft\right) = 33\ in$ $t_c := 3.25\ in$ $d_{flute} := 2\ in$

$C := 0.85 \cdot f'c \cdot b \cdot t_c = (3.647 \cdot 10^5)\ lb$ T > C - slab is inadequate

$A_{sc} := \pi \cdot \left(\frac{3}{8}\ in\right)^2 = 0.442\ in^2$ $n_{studs} := 10$

$Q_{nr} := min\left(0.5 \cdot A_{sc} \sqrt{f'c \cdot E_c}, 0.6 \cdot 1.0 \cdot A_{sc} \cdot f_u\right) = (1.723 \cdot 10^4)\ lb$

$S := \text{floor}\left(\frac{n_{studs}}{2}\right) \cdot Q_{nr} = (8.615 \cdot 10^4)\ lb$ S < min(T,C) - beam is partially composite, PNA is in the steel

$a := \frac{min(T, C, S)}{0.85 \cdot f'c \cdot b} = 0.768\ in$

$y_{PNAguess} := 10\ in$

$f_{web}(y_{PNA}) := fy \cdot t_{web} \cdot \left((y_{PNA} - t_{fl}) - \left((d - 2 \cdot t_{fl}) - (y_{PNA} - t_{fl})\right)\right) - 0.85 \cdot f'c \cdot b \cdot a$

$y_{PNAweb} := \text{root}\left(f_{web}(y_{PNAguess}), y_{PNAguess}\right) = 9.846\ in$

$f_{flange}(y_{PNA}) := fy \cdot \left(b_{fl} \cdot \left(2 \cdot t_{fl} - (d - y_{PNA})\right) + t_{web} \cdot \left(d - 2 \cdot t_{fl}\right) - b_{fl} \cdot \left(d - y_{PNA}\right)\right) - 0.85 \cdot f'c \cdot b \cdot a$

$y_{PNAflange} := \text{root}\left(f_{flange}(y_{PNAguess}), y_{PNAguess}\right) = 11.75\ in$

$y_{PNA} := min\left(y_{PNAweb}, y_{PNAflange}\right) = 9.846\ in$

$$Mn := min(C, S) \cdot \left(d + t_c + d_{flute} - \frac{a}{2} - y_{PNA}\right) + fy \cdot b_{fl} \cdot t_{fl} \cdot \left(d - \frac{t_{fl}}{2} - y_{PNA}\right)$$
$$+ fy \cdot t_{web} \cdot \frac{(d - t_{fl} - y_{PNA})^2}{2} + fy \cdot t_{web} \cdot \frac{(y_{PNA} - t_{fl})^2}{2} + fy \cdot b_{fl} \cdot t_{fl} \cdot \left(y_{PNA} - \frac{t_{fl}}{2}\right)$$

Calculate percent composite before heating

$Composite_{percent} := \frac{min(C, T, S)}{min(C, T)} = 0.236$ $Mn = (2.181 \cdot 10^5)\ lb \cdot ft$

Appendix 2: SFRM Thickness Calculation

W12x26 $d := 12.2\ in$ $bf := 6.49\ in$ $tw := 0.23\ in$

$$D_1 := 2 \cdot d + (3 \cdot bf) - 2 \cdot tw = 43.41\ in$$

D902 Table 6C

Restrained Assembly Rating Hr	Unrestrained Beam Rating Hr	Protection Mil Thkns on Structural Members In: W8x28 When Deck Is All Fluted	W8x28 When Deck Is Fluted or All Cellular	W12x14 When Deck Is All Fluted	Joist (Item 1C or 1D) When Deck Is Fluted Cellular or Bored
1	1	5/16, 7/16"	5/16, 7/16"	1/2,5/8"	9/16
1-1/2	1	5/16, 7/16"	5/16, 7/16"	1/2,5/8"	1
2	1	5/16, 7/16"	5/16, 7/16"	1/2,5/8"	1-3/8
2	2	11/16	13/16	1	1-3/8
2	3	1-1/16	1-5/16	1-1/2	2-1/4

Calculate thickness of the SFRM according to D902, part 6C

W12x14 starting beam

$d := 11.9\ in$ $bf := 3.97\ in$ $tw := 0.2\ in$

$$D_2 := 2 \cdot d + (3 \cdot bf) - 2 \cdot tw = 35.31\ in$$

$w_1 := 26\ \frac{lb}{ft^3}$ $w_2 := 14\ \frac{lb}{ft^3}$ $T_2 := 1\ in$ 2-hr Rest Assembly & 2-hr Unrestrained Beam

Converted W12x26 thickness from ASCE 29-05:

$$T_1 := \frac{\left(\frac{w_2}{D_2} + 0.6\ \frac{lb}{ft^3 \cdot in}\right) \cdot T_2}{\frac{w_1}{D_1} + 0.6\ \frac{lb}{ft^3 \cdot in}} = 0.831\ in$$

Round up to nearest 1/8" - 7/8"

$\frac{7}{8} = 0.875$

W8x28 Alternate starting beam

$d := 8.06\ in$ $bf := 6.54\ in$ $tw := 0.285\ in$

$$D_2 := 2 \cdot d + (3 \cdot bf) - 2 \cdot tw = 35.17\ in$$

$w_1 := 26\ \frac{lb}{ft^3}$ $w_2 := 28\ \frac{lb}{ft^3}$ $T_2 := \frac{11}{16}\ in$

Converted W12x26 thickness from ASCE 29-05:

$$T_1 := \frac{\left(\frac{w_2}{D_2} + 0.6\ \frac{lb}{ft^3 \cdot in}\right) \cdot T_2}{\frac{w_1}{D_1} + 0.6\ \frac{lb}{ft^3 \cdot in}} = 0.801\ in$$

Round up to nearest 1/8" - 7/8"

$\frac{7}{8} = 0.875$

Appendix 3: Shadow Effect Coefficient Calculation

$d := 7.89\ in$ $\quad A := 2.96\ in^2$

$bf := 3.94\ in$

$tf := 0.205\ in$

$tw := 0.170\ in$

Weighted steel areas:

$Af := bf \cdot tf = 0.808\ in^2$ $\quad Aw := A - 2 \cdot Af = 1.345\ in^2$

$\frac{Af}{A} = 0.273$ $\quad \frac{Aw}{A} = 0.454$

Heated perimeter for 3-sided heating:

$Hp := 2 \cdot d + 3 \cdot bf - 2 \cdot tw = 27.26\ in$

Heated perimeter of equivalent box section:

$Hpb := 2 \cdot d + 2 \cdot bf = 23.66\ in$

Overall Shadow Effect Factor for single average steel temperature:

$$k\_sh := \frac{0.9 \cdot \frac{Hpb}{A}}{\frac{Hp}{A}} = 0.781$$

Multiply by total avg. steel temperature to account for shadow effect.

Use weighted areas to apply shadow effect only to web in three-lumped mass calcs:

$$\frac{Af}{A} + \frac{Aw}{A} + \frac{Af}{A} = 1$$

$$\frac{Af}{A} + k\_web \cdot \frac{Aw}{A} + \frac{Af}{A} = k\_sh = 0.781$$

$$k\_web := \frac{k\_sh - 2 \cdot \left(\frac{Af}{A}\right)}{\frac{Aw}{A}}$$

$k\_web = 0.52$

Appendix 4: Truss Finite Element Stiffness Calculation

$E := 210\ GPa$ Elastic Modulus $\nu := 0.3$ Poisson's Ratio

$$G := \frac{E}{2 \cdot (1+\nu)} = 80.769\ GPa$$

$trb := 0.03\ m$ thickness of reaction block

$tlb := 0.056\ m$ thickness of loading block

$$Lb := \frac{1}{2} \cdot (trb + tlb) = 0.043\ m$$ Bolt length at each shear plane

$\beta b := 1$ Concentration of bearing forces correction factor

$$Kbr := \frac{1}{1+(3 \cdot \beta b)} \cdot \frac{(trb \cdot tlb \cdot E)}{2 \cdot (trb + tlb)} = (5.128 \cdot 10^{5})\ \frac{kN}{m}$$

$$\kappa := \frac{1}{\left(\frac{7}{6} + \left(\frac{1}{6}\right) \cdot \left(\frac{\nu}{(1+\nu)}\right)^2\right)} = 0.851$$ Shear Coefficient for circular cross-section

$nsp := 2$ Number of shear planes

1" bolt calcs to verify against reported data in Weigand et al (2018):

$d := 0.0254\ m$

$$Ab := \pi \cdot \left(\frac{d}{2}\right)^2 = (5.067 \cdot 10^{-4})\ m^2$$

$$Ib := \frac{\pi}{64} \cdot d^4 = (2.043 \cdot 10^{-8})\ m^4$$

$$\Phi := \frac{12 \cdot E \cdot Ib}{Lb^2} \cdot \left(\frac{1}{\kappa \cdot G \cdot Ab}\right) = 0.8$$

$$Kv := \frac{12 \cdot E \cdot Ib}{Lb^3 \cdot (1+\Phi)} = (3.598 \cdot 10^{5})\ \frac{kN}{m}$$

$$Ki := \frac{nsp}{\frac{1}{Kbr} + \frac{1}{Kv}} = (4.229 \cdot 10^{5})\ \frac{kN}{m}$$ ambient axial stiffness of one bolt

Reported average of A490 and A325 bolts from Weigand et al (2018): 508,758 kN/m

Measured stiffnesses ranged from 406,246 kN/m to 563,716 kN/m

3/8" bolt calcs based on existing reference values: $nsp := 1$

$d := 0.0095\ m$

$Ab := \pi \cdot \left(\frac{d}{2}\right)^2 = (7.088 \cdot 10^{-5})\ m^2$

$Ib := \frac{\pi}{64} \cdot d^4 = (3.998 \cdot 10^{-10})\ m^4$

$\Phi := \frac{12 \cdot E \cdot Ib}{Lb^2} \cdot \left(\frac{1}{\kappa \cdot G \cdot Ab}\right) = 0.112$

$Kv := \frac{12 \cdot E \cdot Ib}{Lb^2 \cdot (1+\Phi)} = (1.14 \cdot 10^4)\ \frac{kN}{m}$

$Ki := \frac{nsp}{\frac{1}{Kbr} + \frac{1}{Kv}} = (1.115 \cdot 10^4)\ \frac{kN}{m}$ ambient axial stiffness of one bolt in shear tab connection

Calculate required truss area for SAFIR truss representing single bolt:

$L\_truss := 0.1664\ m$

$E\_truss := 500 \cdot 10^9\ Pa$

$A := Ki \cdot \frac{L\_truss}{E\_truss} = (3.711 \cdot 10^{-6})\ m^2$